Topological model of *type II* deformation twinning in 10M Ni-Mn-Ga

BIBEK KARKI a*, PETER MÜLLNER a, ROBERT PONDb

ABSTRACT

The structure of type II twins in 10M Ni-Mn-Ga is modeled using the topological method. This method predicts the same twinning parameters as the kinematic model of Bevis and Crocker. Furthermore, topological modeling provides mechanistic insight into boundary migration rates, the twinning stresses and their temperature dependence. A type II twin is envisaged to form from a precursor, which is its type I conjugate. Disconnections on the precursor \mathbf{k}_1 plane align into a tilt wall, which, after the relaxation of the rotational distortions, forms the type II boundary parallel on average to the \mathbf{k}_2 plane. The component defects may align into a sharp wall or relax by kinking into a less orderly configuration. Both interfaces can host additional glissile disconnections whose motion along a boundary produces combined migration and shear. The ease of motion of these defects increases with their core width, and this, in turn, decreases with increasing sharpness of the boundary. Some experimental evidence in other materials suggests that type II twins can reduce their interfacial energy by adopting a configuration of lowindex facets, which reduces twin boundary mobility. Topological modeling suggests that such a coherently faceted structure is unlikely in 10M Ni-Mn-Ga, in agreement with the high mobility of type II twin boundaries.

1 Introduction

10M Ni-Mn-Ga (hereafter NMG) is a ferromagnetic shape memory alloy which produces force and deformation in response to an applied magnetic field [1–3]. An applied field reorients martensitic variants within the material through the motion of twin boundaries (TBs), causing transformation strains of about 6% with sub-millisecond response times [4–6]. Potential applications include actuation, energy harvesting, vibration damping, and sensing [6–11]. NMG is monoclinic and exhibits compound, *type I*, and *type II* twins [12–16]. Extensive experimental work has established that *type II* TBs have particularly high mobility and low twinning stress, so these twins are especially suitable for the manufacture of high-performance devices [15,16]. Several phenomenological models have been proposed to discuss the difference in boundary mobility of *type I* and *type II* twins [17–21]. The objective of the present work is to elucidate the structure of *type II* TBs, and hence provide some understanding of their exceptional properties.

Twinning has been studied for many decades [22–29], and a theory for predicting their crystallographic forms was developed by Bevis and Crocker [22]; we refer to this kinematic

^a Micron School of Material Science and Engineering, Boise State University

^b College of Engineering, Mathematics and Physical Sciences, University of Exeter

^{*}Corresponding author, email: bkkarki@u.boisestate.edu

treatment as the Classical Model (CM). Further insight into the atomic structure of compound and *type I* twins was accumulated over many years because they are amenable to experimental investigations using techniques such as transmission electron microscopy (TEM) [30–33] and X-ray diffraction [13,15,34]. Boundary planes are rational for compound and *type I* twins, while the twinning direction is rational for the former but irrational for the latter. Of particular relevance to the present discussion, the mechanism of boundary migration for these twins was established to be through the motion of twinning dislocations along a boundary [35]. In a later theory of interfacial defects, called the topological theory [36], these defects were re-named "disconnections" to emphasize that they exhibit both dislocation and step character.

By comparison with compound and *type I* twins, much less is known about *type II* twins [27,30,37]: this is mainly because *type II* TB planes are irrational, which makes TEM and atomic-scale simulations problematic. However, a theoretical model for the formation of *type II* twins was suggested recently [38,39] and shown to be consistent with experimental observations in α – U and NiTi. Disconnection motion and assembly into arrays are central in this model, which we refer to as the Topological Model (TM) [36]. Thus, the principal aims of the present work are to analyze the structure of *type II* twins in NMG using the TM and to investigate boundary migration by disconnection motion. The relative ease with which disconnections move pertains not only to boundary migration rates but also to the magnitude and temperature dependence of twinning stress.

Section 2 is a review of the crystal structure of NMG. It is important to demonstrate that the crystallographic twinning parameters for NMG predicted by the TM are the same as those obtained by the CM. In **Section 3**, we apply the original CM formulation to find all possible conventional twins in NMG. The *type II* TB structure, according to the TM, is described in **Section 4**. Three alternative boundary structures are proposed, and their differing migration rates and twinning stresses are discussed in **Section 5**. **Section 6** is a summary of our conclusions.

2 CRYSTALLOGRAPHY OF NI-MN-GA

In our analysis, we refer to the axis systems with subscript c, 10M, and m, for the cubic austenite structure, the modulated monoclinic martensite structure, and the approximated monoclinic martensite structure, respectively.

2.1 AUSTENITE CRYSTAL STRUCTURE AND SYMMETRY

Above the martensitic transformation temperature, stoichiometric Ni_2MnGa is a L2₁-ordered Heusler alloy exhibiting symmetry of space group $Fm\overline{3}m$ [40]. The atomic motif is Ga at 0,0,0, Mn at 0,0.5,0, and Ni at 0.25,0.25,0.25 and 0.25,0.25,0.75 at each lattice point, as illustrated

in Figure 1 (a). The near-stoichiometry alloy with nominal composition $Ni_{50}Mn_{25+x}Ga_{25-x}$ (at.%), with x often between 2 and 4, exhibits modulated martensite structure with highly mobile TBs [13,41]. In the present work, we refer specifically to the alloy $Ni_{50.2}Mn_{28.3}Ga_{21.5}$, with the lattice parameter $a_c=0.5832$ nm and martensite transformation temperature $M_s=323$ K [13].

2.2 MODULATED MARTENSITE STRUCTURE AND SYMMETRY

Following a martensitic transformation, the symmetry of the alloy reduces to monoclinic (space group I2/m [42]). A schematic illustration of the martensite viewed along its unique axis $[010]_{10M}$ is shown in Figure 1 (b), including an outline of the unit cell with lattice parameters a_{10M} , b_{10M} , c_{10M} , and β_{10M} . In this diagram, we see the modulated structure of the crystal, designated 10M, where these modulations have formed by a simple shear along $\{220\}_c$ planes of the parent FCC unit cell. The repeating sequence of shears between adjacent planes is three leftwards followed by two rightwards, and they are characterized as $(\bar{3}2)_2$ to emphasize the ten-layer sequence. An electron diffraction pattern obtained with the beam direction $[010]_{10M}$ (i.e., parallel to the $\{220\}_c$ planes, Figure 1 (c)) exhibits fundamental and superlattice reflections. Atomic positions in the actual martensite structure may not correspond exactly to the configuration in Figure 1 (b), and alternative atomic displacements parallel to these $\{220\}_c$ are discussed elsewhere [12,43,44].

2.3 APPROXIMATED MONOCLINIC STRUCTURE AND SYMMETRY

To assist the crystallographic analysis of twinning in NMG, we adopt the suggestions of Sozinov et al. [13,15] whereby a non-conventional monoclinic unit cell is established by suppressing the modulation evident in Figure 1 (c) and considering only the fundamental reflections. This unit cell is derived from the cubic form in Figure 1 (a) by a monoclinic distortion with lattice parameters a_m , b_m , c_m and γ_m . The systematic offset of $\{220\}_c$ planes in the modulated martensite are averaged in this visualization: the 10M sequence now is $(1)_{10}$ rather than $(\bar{3}2)_2$.

The point symmetry of this non-conventional face-centered monoclinic unit cell is 2/m as illustrated in projection along its unique axis, $[001]_m$, in Figure 1 (d). Using X-ray diffraction, Sozinov et al. [15] determined the lattice parameters for $Ni_{50}Mn_{28.5}Ga_{21.5}$ (±0.2 at.%) as $a_m=0.5974$ nm, $b_m=0.5947$ nm, $c_m=0.5581$ nm and $\gamma_m=90.36^\circ$. Transformation matrices interrelating planes and directions in 10M and m crystals are set out in Appendix A.

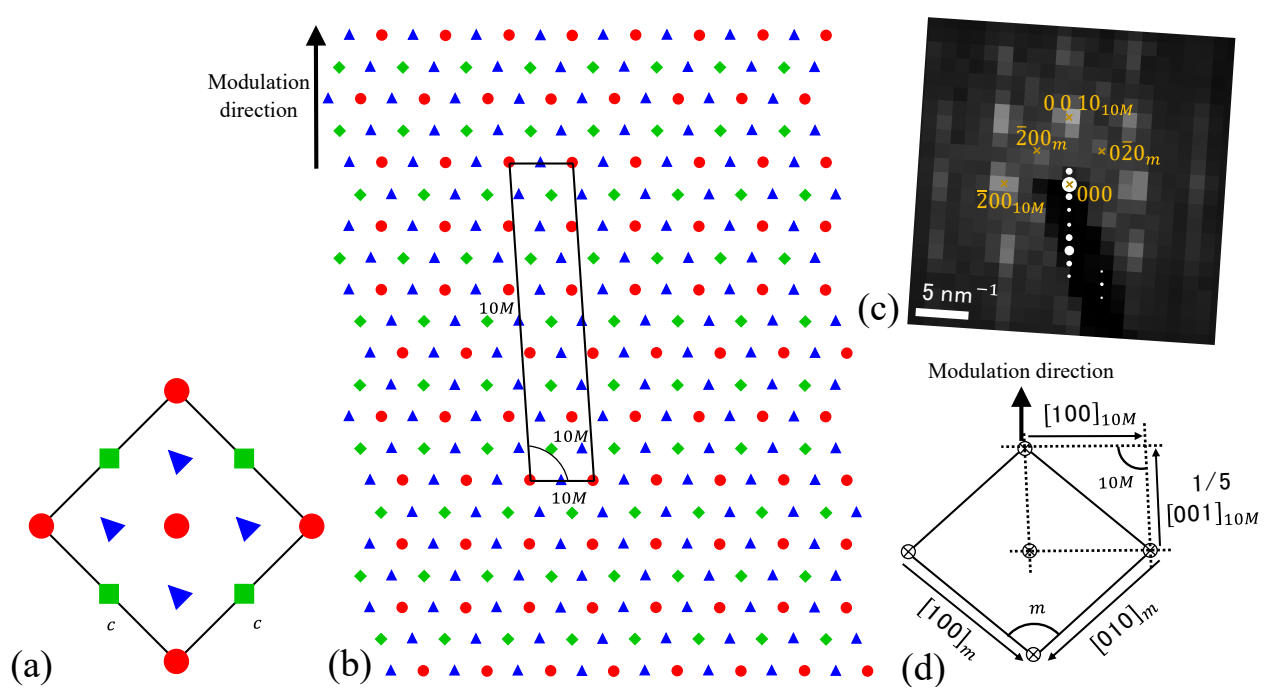


Figure 1: (a) Austenite crystal structure of stoichiometric Ni_2MnGa viewed along one of its axes. Red is Gallium (circle), green is Manganese (square), and blue is Nickel (triangle). (b) The crystal structure of 10M Ni-Mn-Ga (NMG) viewed along its unique axis $[010]_{10M}$ shows the modulated assembly of the crystal; a periodic simple shear along $\{220\}_c$ planes achieves modulation during the martensitic transformation. The monoclinic angle, β_{10M} , is exaggerated in the current illustration. (c) Experimentally observed diffraction pattern of NMG that corresponds to the schematic illustration in (b): the superlattice reflections correspond to the periodic offset of the $\{220\}_c$ planes. (d) Approximated NMG crystal lattice using only the fundamental reflections in (c) and derived from the parent cubic axes through a monoclinic distortion.

3 THEORIES OF DEFORMATION TWINNING

3.1 CLASSICAL MODEL

A comprehensive review of the CM of deformation twinning has been presented by Christian and Mahajan [27] and is briefly summarized here. When a medium is deformed by a volume conserving homogeneous plane strain shear, two mutually conjugate planes k_1 and k_2 , inclined by an angle 2ϕ , remain undistorted, as illustrated in Figure 2 (a). The plane of shear is designated P_s , and its normal is n_s . When the plane of shear is irrational, one of the undistorted planes is rational (defined as k_1), and the other is irrational (defined as k_2) [23,24]. If the deformed crystal is further rotated by an angle $\alpha=\pm(\pi/2-2\phi)$ about n_s , one of the conjugate planes comes into coincidence with its orientation before deformation, thereby becoming the invariant plane of twinning. If k_1 is brought into coincidence by rotation, the invariant plane is rational, as illustrated in Figure 2 (b); conversely, if k_2 is brought into coincidence, the invariant plane is irrational.

In both cases, the overall deformation is a simple shear. The directions parallel to k_1 and k_2 , which also lie in P_s , are designated γ_1 and γ_2 respectively. The magnitude of shear is s=

 $2cot2\phi$, parallel to either γ_1 or γ_2 . When the invariant plane is rational, the twins are designated $type\ I$, and the orientation relationship between the matrix and twin crystal is mirror reflection across k_1 , denoted by m', where the prime indicates a "color-reversing" symmetry operation [45,46]. The conjugate of a $type\ I$ twin, i.e., where the invariant plane is parallel to k_2 , is called $type\ II$, and the operation interrelating the crystals is 2' about γ_2 . In centrosymmetric crystals such as NMG, the interrelationship for $type\ I$ twins can be equivalently described as 2' about the vector normal to k_1 , and for $type\ II$ twins as m' across the plane normal to γ_2 . A third kind of twin called compound arises when all the twinning elements $-P_s$, n_s , k_1 , k_2 , γ_1 and γ_2 are rational. There is a fourth kind of twin called nonconventional where P_s and n_s are rational, but k_1 , k_2 , γ_1 and γ_2 are irrational. Such twins have been observed in composite arrangements of compound twins [47] but are not pertinent to the present study. Frank [24] suggested that an experimentally observed twinning mode be characterized by parameters K, η , as shown in Figure 2 (c).

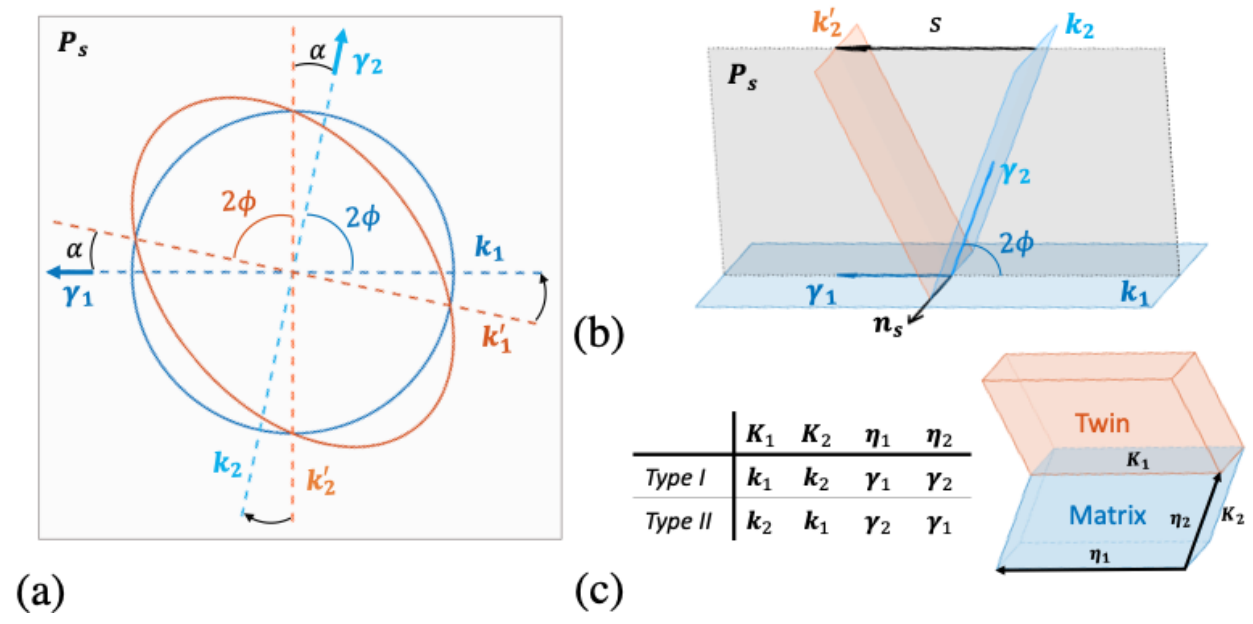


Figure 2: (a) A volume conserving plane-strain deformation shows two undistorted planes k_1 and k_2 that are simply rotated in the deformed medium (k_1' and k_2'). (b) The k_1 plane becomes the invariant plane of twinning when the deformed medium in (a) is further rotated by $+\alpha$ about n_s (c) An illustration of experimentally observed twinning parameters K and η : the inset table shows their relationship with twinning elements described in the text. The table also shows the conjugate relation between $type\ l$ and $type\ ll$ twins.

The geometrical parameters and shear magnitudes for conjugate twinning modes can be predicted theoretically [22,25–27,29]. In the present work, we use the approach developed by Bilby and Crocker [26] and Bevis and Crocker [22,29], where the parameters are deduced from the elements of correspondence matrices. In the present case, where the monoclinic unit cell is

obtained by a small distortion of the cubic cell, correspondence matrices conform to cubic symmetry operations that are suppressed by this distortion.

3.2 TOPOLOGICAL MODEL

While the CM evaluates the geometrical parameters defining a twinning mode, it fails to provide insight into the mechanism of formation and growth of twins. The study of twinning dislocations has led to a better understanding of the twinning mechanism [27]. Pond, Hirth, and co-workers [35,36,45,46] extensively studied the character of interfacial defects and presented a TM, which rigorously characterizes the dislocation and step character of twinning defects. Because of this dual topological character, twinning defects are referred to as disconnections, exhibiting both Burgers vector, \boldsymbol{b} , and step height, \boldsymbol{h} . In the literature, there are many accounts of disconnections in *compound* twins [35,48–52]. In compound and *type I* twins, the motion of a disconnection along the $\boldsymbol{K}_1 = \boldsymbol{k}_1$ plane produces an engineering shear, $\gamma_e = b/h$, which has the same magnitude as the classical value, s, and is parallel to the classical shear direction, $\eta_1 = \gamma_1$. In addition, the nucleation and growth of *type I* and *compound* twins in terms of disconnection generation and motion have been modeled consistently with experimental observations [52–54]. Figure 3 is a schematic illustration of *type I* twins nucleated at a crystal surface source and growing into the bulk during compressive loading of NMG. The Burgers vector \boldsymbol{b} is shown for the line sense $\boldsymbol{\xi} \parallel \boldsymbol{n}_s$ pointing out of the page.

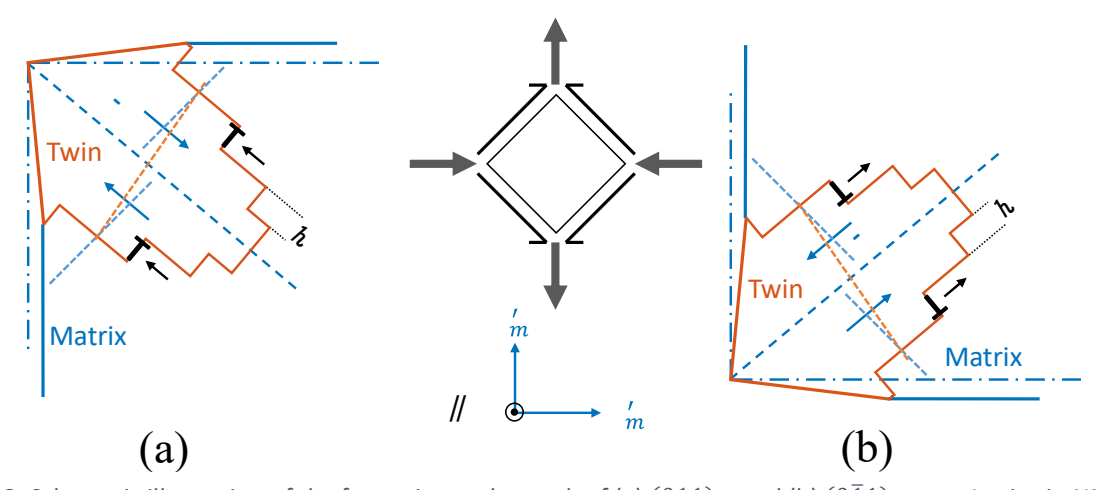


Figure 3: Schematic illustration of the formation and growth of (a) $(011)_m$ and (b) $(0\bar{1}1)_m$ type I twins in NMG under compressive load. The disconnections (b,h) nucleate near the corner of parallelepiped specimen and propagate into the bulk by gliding along k_1 planes. The disconnection line sense $\xi \parallel n_s$ points out of the page.

In contrast, our knowledge of the formation and growth of *type II* twins is less developed. Recently, Pond and Hirth [38] presented a model in the framework of the TM that provides insight into the formation of *type II* twins; we apply this model to the case of NMG. Figure 4 is a schematic depiction of the formation of the *type II* twin during compressive loading of NMG.

The $(q_1\bar{1}1)_m$ type I twin shown in Figure 4 is the conjugate of the $(011)_m$ type I twin shown in Figure 3 (a). Initially the disconnections (b,h) are generated at a surface source and propagate into the bulk by gliding along the k_1 planes (Figure 4 (a)), tending to form a lenticular twin tip. However, if the leading disconnections begin to accumulate on the plane perpendicular to k_1 , Figure 4 (b), they would gradually form a planar boundary in which the step character of the component defects has been lost. Each defect in this array produces a displacement field comprising both strain and rotational distortions. As the configuration relaxes, the strain field parallel to the final interface, Figure 4 (c), vanishes at long range. At the same time, the rotation field, which sums to produce a rotation of 2α about n_s , partitions symmetrically between the adjacent crystals: the rotation of the twin crystal is unconstrained because of the free surfaces. At equilibrium, the interface plane rotates relative to the fixed matrix crystal by α about n_s and hence becomes parallel to k_2 , i.e. the type II conjugate has formed with interface $K_1 = k_2$, as shown in Figure 4 (c).

We propose that the tip blunting of the initial *type I* twin occurs because of the stress-state imposed to induce twinning in single crystal specimens: for example, one method involves bending the specimen [90]. This would produce an inhomogeneous stress field: compressive in the upper region of the specimen but tensile in the lower part, as indicated schematically by the stress figures in Figure 4 (e). Thus, the leading disconnections would experience a diminishing driving force as they approach the neutral plane, and an opposing force thereafter. Furthermore, it is known that in a homogeneous stress field, the force necessary for an additional dislocation to join a tilt wall diminishes as the wall lengthens [55,56]. We emphasize that specimen bending induces twin nucleation and formation of type II twin: once the type II twin has been introduced in this manner, its dynamic properties are studied by the application of a homogeneous compressive or tensile stress to the specimen.

The defect structure of a sharp $type\ II$ interface viewed along the direction $\xi \parallel n_s$ is schematically illustrated in Figure 4 (d). The step character of individual defects is lost, and there is no residual component of ${\bf b}$ along ${\bf k}_2$. Thus, the tilt array can be envisaged as a wall of grain boundary dislocations with Burgers vector ${\bf b}^g={\bf b}\cos\alpha$ and spacing $h/\cos\alpha$. Hence from the geometry of Figure 4 (d) we see that $\alpha=\tan^{-1}(b/2h)$: using the magnitudes for $|{\bf b}|$ and h listed in Section 4.2, we find $\alpha=3.64^\circ$, which is the same as the value obtained from the CM. Thus, the total misorientation across the boundary is the combination of the $type\ I$ misorientation, n_{k_1}/π , with the supplementary tilt, $n_s/2\alpha$. This combination brings the $[011]_m$ directions of the two crystals into coincidence, thereby forming the $\eta_1=\gamma_2$ direction. Thus, the final misorientation can be expressed as γ_2/π , or as a γ_2/π axis along this direction interrelating the two crystals. While the long-range strain field of the sharp interface vanishes, we presume that its core energy may be substantial because the component defects in Figure 4

(c) lie on adjacent k_1 planes. Atomic scale simulations are required to determine such energies, but this is beyond the scope of the present work. Some authors [27,30,57–60] have suggested the twin interface may reconfigure into rational facets lying in the $\eta_1=\gamma_2$ zone: this possibility is investigated further in Appendix C. Pond and Hirth [38] suggested another relaxation mechanism where the core energy of the defects diminishes by kinking into rational segments while retaining the average line direction, $\overline{\xi} \parallel n_s$. Since the kinked defects retain the overall average line direction, they do not produce a long-range strain field; nonetheless, a strain field arises near the interface extending to a distance on the order of the kink length. Such a kinked configuration might also affect the mechanism and kinetics of interface migration in response to an applied driving force, as is explored later.

When twin nucleation occurs in the bulk, it has been suggested [38] that whether the *type I* or the *type II* conjugate forms is the outcome of a competitive process. The model is consistent with experimental findings where predominantly either a *type I* or a *type II* twin forms [38,39]. However, experimental observations of NMG [19,61,62] show that non-conjugate *type I* and *type II* pairs of twins are sometimes observed following surface nucleation, implying that the activation energy of both processes may be similar. In the present article, our focus is the difference in mobility between *type I* and *type II* twins.

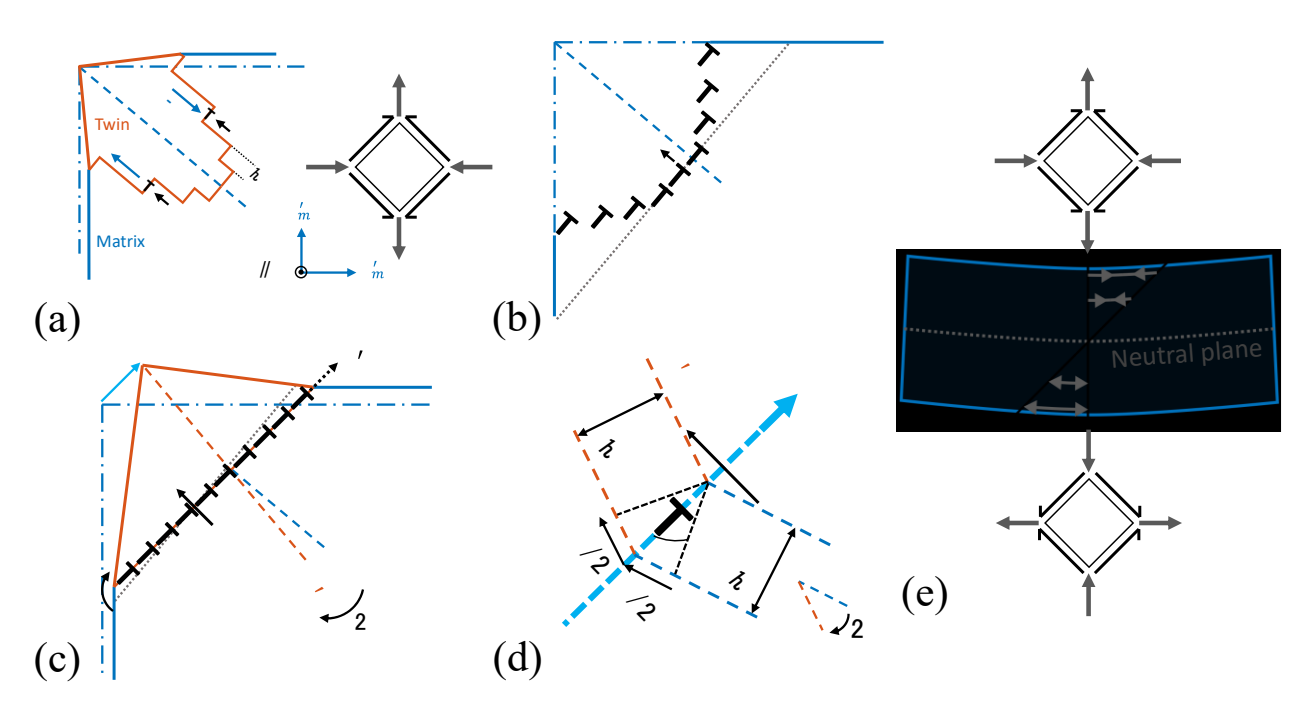


Figure 4: Schematic illustration of the formation of $(q_1\overline{1}1)_m$ type I1 twins in NMG. (a) Initially, nascent $(011)_m$ type I2 disconnections nucleate at the surface source in response to a local compressive stress. (b) The notional intermediate stage in an inhomogeneous stress field due to specimen bending: here the disconnections begin to accumulate and form a tilt wall perpendicular to the glide plane \mathbf{k}_1 . (c) Finally, a $(q_1\overline{1}1)_m$ type II2 conjugate is formed after symmetrical partitioning of the rotational distortions across the tilt wall. (d) The exploded view of the sharp type II3 interface in (c), showing the character of the defects in the array: $\mathbf{b}^g = \mathbf{b} \cdot cos\alpha$ is the resultant

Burgers vector of each grain boundary dislocation. (e) The stress distribution in a bent parallelepiped specimen showing the stress reversal across the neutral plane, which promotes tip blunting.

4 STRUCTURAL MODELS OF TYPE II TWINS IN NMG

4.1 Previous Investigations

Researchers have investigated the structure of *type II* twins in NMG using a variety of experimental techniques. While observations using optical microscopy [13,63], X-ray diffraction [13,15,64,65], and electron diffraction [14,16,66] are consistent with the twinning parameters predicted by the CM, the atomic structure of *type II* twins is not yet established. Based on high-resolution transmission electron microscopy (HRTEM) observations, there are two opposing conjectures:

- a) The TB is inherently irrational, and thus we find randomly curved strain contrast along the boundary in HRTEM images [31,37,66,67].
- b) The TB consists of terraces of a nearest low-index rational plane with periodic step-like features. The overall boundary is close to the predicted irrational plane [27,30,57–60].

Matsuda et al. [66] employed HRTEM to study various twins including the *type II* twinning mode in NMG with $\eta_1 = \langle \bar{5}\bar{5}1 \rangle_{10M} = \langle \bar{1}0\bar{1} \rangle_m$. Although the authors were able to simultaneously resolve lattice fringes of the adjacent crystals, the boundary was not oriented edge-on to the beam, and thus image interpretation was difficult. Moreover, no step-like line-defects were discerned.

Müllner [68] adopted the TM of *type II* boundaries and showed that disconnection loops can be formally defined on the irrational boundary based on the elastic properties of crystals. Moreover, using this formalism, Müllner described the difference in twinning stress and the impact of temperature on the twinning stress of *type I* and *type II* boundaries.

Knowles and Smith [69] investigated [011] type~II TBs in a monoclinic NiTi using TEM, and noted that the common $(11\bar{1})$ planes are inclined at $10\pm2^\circ$ to $\pmb{K}_1=\pmb{k}_2$. Later, using HRTEM, Knowles [30] proposed that these TBs may be composed of a combination of $(11\bar{1})$ and $(01\bar{1})$ facets. Further investigation by Liu and Xie [57,58] using HRTEM combined with image simulation reached similar conclusions.

4.2 CRYSTALLOGRAPHY OF TWINS IN NMG

The crystallographic parameters predicted by the CM of twinning in NMG are set out in Appendix B. The point symmetry of monoclinic NMG martensite and of the cubic parent phase are 2/m (order 4) and $m\bar{3}m$ (order 48). Therefore, we obtain twelve monoclinic variants interrelated by the symmetry operations of the parent group, which are suppressed by the

monoclinic deformation. These operations define correspondence matrices, C_i , from which the twinning parameters are deduced. The predicted twinning modes are presented in Table 1.

Table 1: Crystallographic parameters of twinning modes in NMG expressed in the approximated martensite framework. The shear values, s, and non-integer coefficients q and r are obtained using the lattice parameters determined by Sozinov et al. [15].

Twin Type	k_1	k_2	γ_1	γ_2	S
Compound	$(110)_m$	$(\bar{1}10)_m$	$[\overline{1}10]_m$	$[110]_{m}$	0.0091
Compound	$(010)_m$	$(100)_m$	$[100]_m$	$[110]_m$ $[010]_m$ $[011]_m$ $[0\overline{1}1]_m$	0.0126
	$(011)_m$	$(q_1\bar{1}1)_m$	$[r_1\overline{1}1]_m$	$[011]_m$	0.1274
type I &	$(0\overline{1}1)_m \qquad (\overline{q_1}11)_m \qquad [\overline{r_1}11]_m \qquad [0\overline{1}1]_m$	$[0\bar{1}1]_m$	0.1274		
∝ type II	$(101)_m$	$(\bar{1}q_21)_m$	$[\bar{1}r_21]_m$	$[101]_m$	0.1365
	$(\bar{1}01)_m$	$(1\overline{q_2}1)_m$	$[1\overline{r_2}1]_m$	$[\overline{1}01]_m$	0.1365

$$q_{1} = \frac{2 a_{m} b_{m} \cos \gamma_{m}}{c_{m}^{2} - b_{m}^{2}} \qquad r_{1} = \frac{2 b_{m} c_{m}^{2} \cos \gamma_{m}}{a_{m} (c_{m}^{2} - b_{m}^{2} \sin^{2} \gamma_{m})}$$

$$q_{2} = \frac{2 a_{m} b_{m} \cos \gamma_{m}}{c_{m}^{2} - a_{m}^{2}} \qquad r_{2} = \frac{2 a_{m} c_{m}^{2} \cos \gamma_{m}}{b_{m} (c_{m}^{2} - a_{m}^{2} \sin^{2} \gamma_{m})}$$

Using the lattice parameters of Sozinov et al. [15], as listed in **Section 2**, the values of the irrational indices are $q_1 = 0.1058$, $q_2 = 0.0983$, $r_1 = 0.0924$ and $r_2 = 0.0866$.

The Burgers vector and step height, (\boldsymbol{b},h) , of defects separating energetically degenerate regions of an interface (designated admissible defects) are obtained using the topological theory of interfacial defects [45,46], which is based on the fundamental principles of symmetry breaking. It is found that the Burgers vector of admissible disconnections correspond to differences between translation vectors in the adjacent crystals: thus, Burgers vectors, expressed in the parent coordinate frame, are given by:

$$\mathbf{b} = \mathbf{P}^{-1}\mathbf{t}(\lambda) - \mathbf{t}(\mu) \tag{1}$$

where $t(\lambda)$ and $t(\mu)$ are translation vectors of the upper (twin) and the lower (matrix) crystal, as in Figure 5, and P represents the coordinate transformation from the μ to λ frame. In the present case, we take P to correspond to an operation of the form 2', as defined in Section 3: thus, for $type\ I$ boundaries, P(I) corresponds to n_{k_1}/π , and for $type\ II$, P(II) corresponds to γ_2/π . The Burgers vector of perfect interfacial defects are independent of the relative position of the adjacent crystals, designated p in the formal theory [45,46]. However, the magnitudes of atomic shuffles accompanying disconnection motion do depend on p, as described elsewhere [52,54]. The step height of a glissile twinning disconnection, h, is given by,

$$h = \mathbf{n} \cdot \mathbf{P}^{-1} \mathbf{t}(\lambda) = \mathbf{n} \cdot \mathbf{t}(\mu) \tag{2}$$

where n represents the unit vector normal to the twin interface. For disconnections in $type\ l$ boundaries, h also corresponds to an integral number of lattice plane spacings parallel to the interface, i.e., $h=n\cdot d_{k_1}$, where n is an integer, and d_{k_1} is the interplanar spacing of the k_1 lattice planes, as illustrated schematically in Figure 5 (a).

Equations (1) and (2) are derived from fundamental principles of symmetry breaking [45,46], so are also valid for disconnections in irrational $type\ II$ boundaries. Admissible defects now separate energetically degenerate regions which are locally isomorphic. Table 2 lists the smallest magnitude values of (b,h) for disconnections in selected examples of all three types of TBs specified in Table 1. The corresponding engineering shear values, γ_e , are the same as the values from the CM, and we note that the magnitudes of γ_e for disconnections in conjugate interfaces are equal. Moreover, the Burgers vectors are parallel to the relevant η_1 . The disconnection depicted in Figure 5 (b) exhibits the topological properties, (b,h), listed in Table 2, where h is understood as the offset in a $type\ II$ boundary. Motion of this glissile disconnection along a k_2 boundary would produce coupled shear and migration, manifested macroscopically as the engineering shear, γ_e . If in reality a defect is less localized, its topological properties remain unchanged overall. More complex perturbations of a $type\ II$ boundary can be envisioned, and can be modeled for example in terms of disconnection dipoles [70,71].

Table 2: Topological parameters used to characterize the disconnections in compound, *type I* and *type II* interfaces. In the formulation of Burgers vectors, the twin (λ) is assumed to be above the matrix (μ) , and the result is expressed in the matrix coordinate frame.

Twin Type	K_1	η_1	$t(\mu)$	$t(\lambda)$	b	b (nm)	h (nm)	γ_e
Compound	$(110)_m$	$[\bar{1}10]_m$	$^{1}/_{2}[101]_{m}$	$^{1}/_{2}[01\bar{1}]_{m}$	$\begin{bmatrix} \overline{0.0023} \\ 0.0023 \\ 0 \end{bmatrix}_m$	0.0019	0.2101	0.0091
	$(010)_m$	$[100]_{m}$	$^{1}/_{2}[011]_{m}$	$^{1}/_{2}[01\bar{1}]_{m}$	$\begin{bmatrix} 0.0063 \\ 0 \\ 0 \end{bmatrix}_m$	0.0037	0.2973	0.0126
Туре І	$(011)_m$	$[r_1\overline{1}1]_m$	$^{1}/_{2}[110]_{m}$	$\frac{1}{2}[\overline{1}01]_m$	$\begin{bmatrix} \frac{0.0029}{0.0317} \\ 0.0317 \end{bmatrix}_m$	0.0259	0.2035	0.1274
	$(101)_m$	$[\overline{1}r_21]_m$	$^{1}/_{2}[110]_{m}$	$^{1}/_{2}[0\bar{1}1]_{m}$	$\begin{bmatrix} \overline{0.0340} \\ 0.0029 \\ 0.0340 \end{bmatrix}_{m}$	0.0278	0.2039	0.1365
Type II	$(q_1\bar{1}1)_m$	$[011]_m$	$\frac{1}{2}$ $[\overline{1}01]_m$	$^{1}/_{2}[110]_{m}$	$\begin{bmatrix} 0 \\ 0.0284 \\ 0.0284 \end{bmatrix}_m$	0.0231	0.1815	0.1274
	$(\overline{1}q_21)_m$	$[101]_m$	$\frac{1}{2}[0\bar{1}1]_m$	$^{1}/_{2}[110]_{m}$	$\begin{bmatrix} 0.0306 \\ 0 \\ 0.0306 \end{bmatrix}_m$	0.0250	0.1835	0.1365

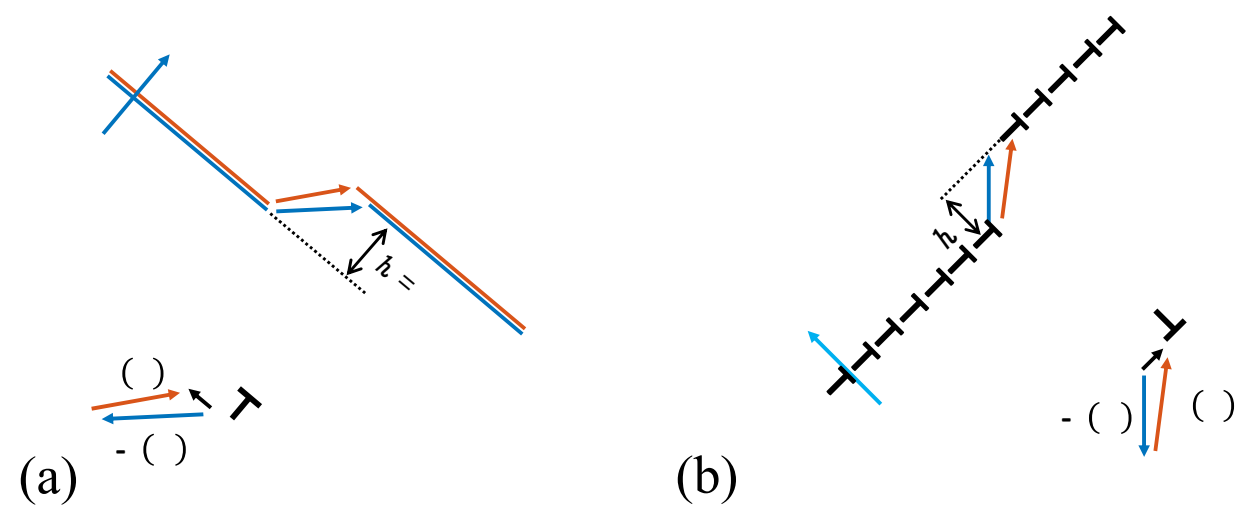


Figure 5: Schematic illustration of a disconnection in (a) $(011)_m$ type I twin interface, and (b) $(q_1\bar{1}1)_m$ type II twin interface.

4.3 INTERFACE MODELS

The sharp interface model of type II boundaries is illustrated in Figure 4 (d). Here, the defects have irrational line direction, $\xi \parallel n_s$, and are spaced $h/\cos \alpha$ apart. In a possible relaxed structure, the disconnections in the glide plane $m{k}_1$ are kinked into rational segments to minimize their line energy [38] (Figure 6). In the present case, where $k_1 = (011)_m$ and $k_2 =$ $(q_1\overline{1}1)_m$, the average line sense, $\pmb{\xi}\parallel\left[1\ q_1/2\ \overline{q_1/2}
ight]_m$ can be approximated as $pprox 10[100]_m+$ $1/2 [01\overline{1}]_m$. These two line segments lie in the $(0\overline{1}1)_m$ and $(\overline{1}00)_m$ planes respectively, which are common to both the twin and matrix as they belong to the $\eta_1 = [011]_m$ zone. Since the k_1 planes are misaligned by 2α about $m{n}_s$, the $[100]_m^\mu$ and $[\overline{1}00]_m^\lambda$ directions are not parallel, and neither are $[01\overline{1}]_m^\mu$ and $[0\overline{1}1]_m^\lambda$, as illustrated in Figure 6 (a). In the case of ordered line segments, as illustrated in Figure 6 (b), where one segment is aligned with those above and below it in the array, the boundary is wider than the sharp ${m k}_2=(q_1\bar{1}1)_m$ form because $[100]_m^\mu$ is inclined by 4.13° to n_s . The kinked configuration does not exhibit a long-range displacement field, although short-range stresses arise. One can imagine less ordered defect configurations where the component line segments are of different lengths and not completely aligned in the array, as shown in Figure 6 (c). Also, in this situation, no long-range displacement field arises, but short-range stresses appear depending on the degree of disorder. We refer to such relaxed structures as ragged type II boundaries (Figure 6) in contrast to the sharp interface depicted in Figure 4 (c) and (d).

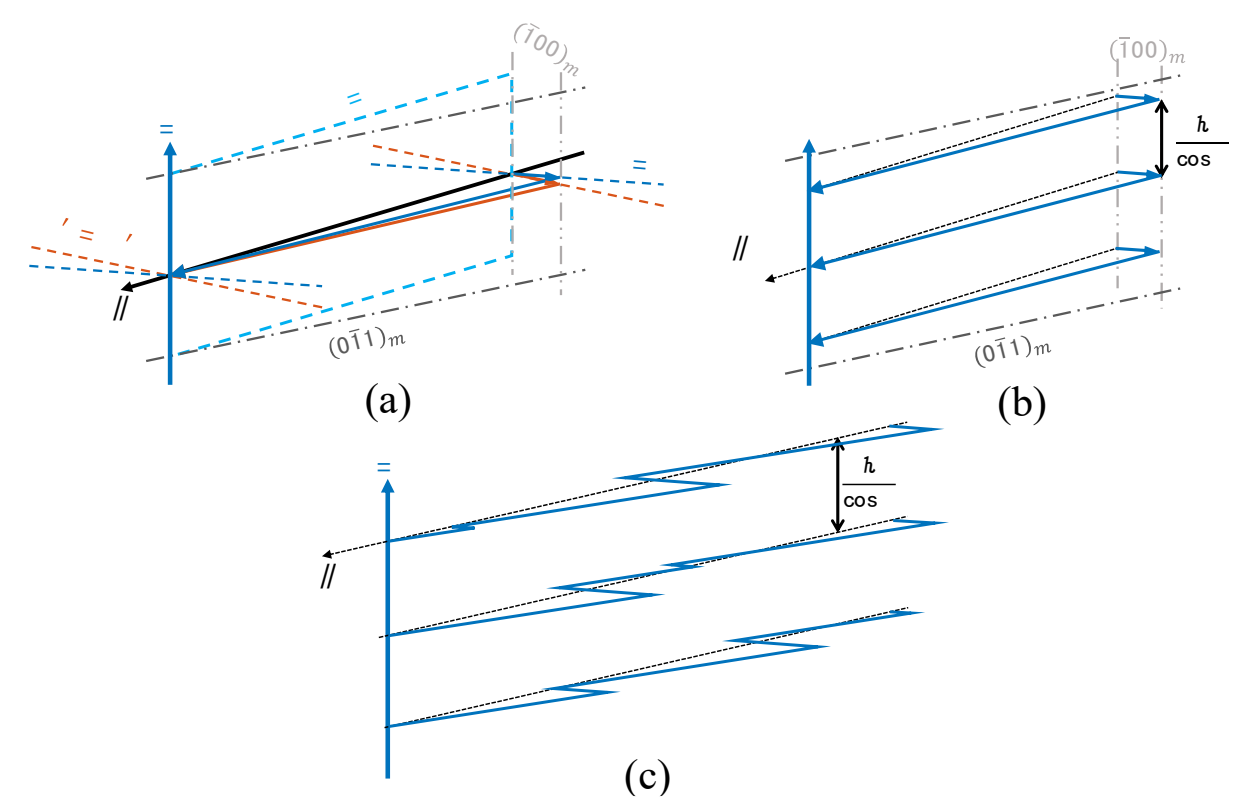


Figure 6: (a) Schematic illustration of defect kinking along low energy Peierls valleys in a $(q_1 \bar{1}1)_m$ type II twin. Here, $\xi \parallel n_s = \left[1 \ q_1/2 \ \overline{q_1/2}\right]_m \approx 10[100]_m + 1/2 \ [01\bar{1}]_m$. (b) An orderly array of aligned kinked defects. (c) A disorderly array of non-aligned kinked defects.

All planes in the η_1 zone are common to the parent and twin crystals: thus, a diffraction pattern taken with the beam along η_1 resembles one of a single crystal [31,37,66,69]. However, these common planes are rationally commensurate only in the η_1 direction [27]: an example is illustrated in Figure 7 (a) for the common $(0\bar{1}1)_m$ planes. An engineering coherency shear strain of magnitude 0.0092 parallel to η_1 would bring $[100]_m^\mu$ and $[\overline{1}00]_m^\lambda$ into parallelism, thereby creating fully coherent $(0\bar{1}1)_m$ planes, as seen in Figure 7 (b). These planes are inclined by only 4.12° to the k_2 planes and may exhibit relatively modest interfacial energy. The coherency strain produces a long-range displacement field unless an interfacial defect array compensates this field. We refer to such an interface structure as being a (misfit-relieved) coherent (low-index) approximant. The immediate vicinity of such a faceted boundary resembles a compound twin with a coherent rational interface and a rational twinning direction. In the published HRTEM images of type II boundaries in NMG [66], step-like defects were not discernible due to the local strain field, so direct experimental of the approximant structure is not available. In Appendix C, we show that in NMG the coherency strain can be accommodated by an array of admissible screw disconnections with $b \parallel [0\overline{1}\overline{1}]_m$. However, the sign of the steps associated with these disconnections causes the average orientation of the faceted configuration to rotate away from k_2 rather than towards it.

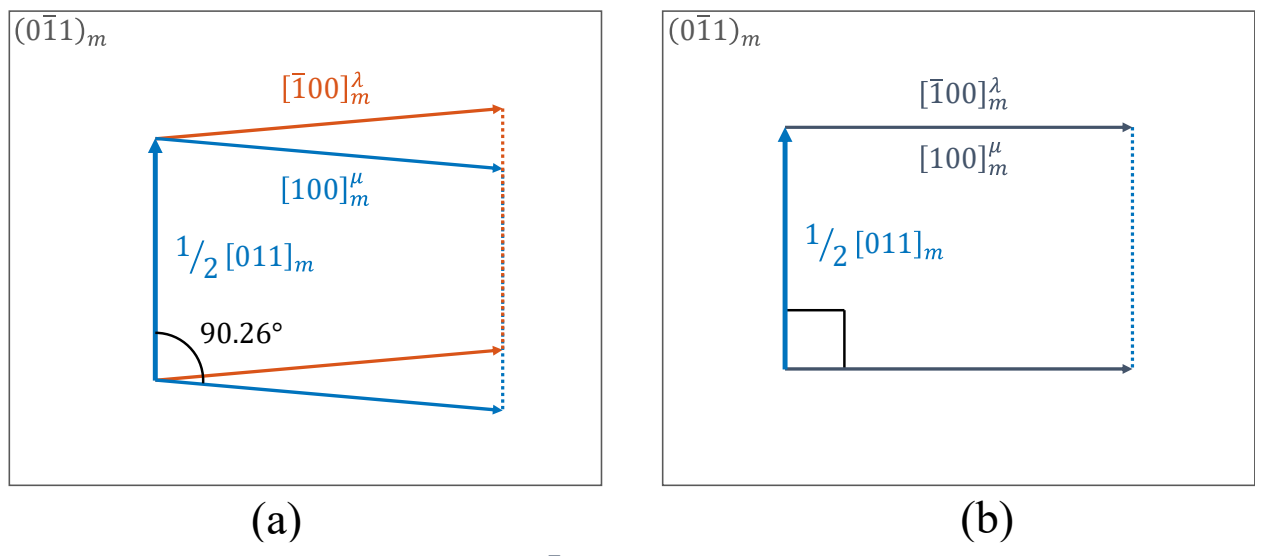


Figure 7: Schematic illustration of the common $(0\bar{1}1)_m$ planes (a) before and (b) after they are sheared into 2-D coherency. In (a), the angle between $[100]_m^\mu$ and $[\bar{1}00]_m^\lambda$ (in reality only 0.52°) is exaggerated. The partitioning of coherency strain between the μ and λ crystals results in $[100]_m$ and $[011]_m$ becoming orthogonal.

5 DISCUSSION

5.1 PROPERTIES OF TYPE I AND TYPE II TWINS

Experimental observations indicate that the physical properties of $type\ I$ and $type\ II$ twins differ, notably in NMG [3,61,65,72]. Earlier works have developed phenomenological descriptions of the observed kinetic behavior of twins: for example, Faran and Shilo [73] found experimentally that the behavior is bimodal, and formulated an expression relating the velocity of a propagating boundary to the thermodynamic driving force. At driving forces below a threshold value, g_o , they propose that motion is governed by thermally activated motion of disconnections, and invoke a mobility coefficient. Above g_o , disconnection motion is modeled as athermal. In later experiments by Saren and colleagues [74,75], bimodal kinetic behavior was not observed, and the authors pointed out the importance of avoiding any mechanical constraints in the experimental apparatus, and also taking the inertia of the growing twin into account when modeling. On this basis, they derived a differential equation relating velocity to magnetic driving force, while incorporating the material's density and specimen geometry.

Here, building on these empirical studies, we outline aspects of disconnection motion in *type I* and *type II* twins which are relevant to the development of a mechanistic understanding of boundary kinetics. In particular, we consider the twinning stress for *type I* and *type II* twins and their dependence on temperature, $\sigma_I^t(T)$ and $\sigma_{II}^t(T)$, respectively. Twinning stress is the stress required to sustain TB motion [76]. In the case of *type I* TBs, the basic mechanism of twinning is the motion of glissile disconnections along low-energy, sharp interfaces [52–54]. Here, we explore the possibility that a similar mechanism operates for *type II* twins, considering that a

twin interface may be (a) a relatively high-energy, sharp interface, (b) a disordered arrangement of kinked disconnections, or (c) a coherently faceted interface. Extrinsic microstructural features such as magnetic domain interactions [77] and junctions between compatible twins influence disconnection motion [34,78]. For simplicity, we neglect such extrinsic effects here, and consider only effects on the disconnection mobility intrinsic to the interface structure.

The two primary features governing TB mobility are the nucleation rate, \dot{N} , of glissile disconnections at a given applied stress and the twin growth rate, \dot{G} , perpendicular to the boundary. For homogenous nucleation of disconnection loops, the activation energy at a fixed stress is to first order proportional to the magnitude of $|\boldsymbol{b}|^2$. As such, thermal activation contributes significantly to \dot{N} at modest stresses because of the small magnitude of Burgers vectors of twinning disconnections [79]. \dot{G} is expected to be dominated by the disconnection mobility. The Peierls stress necessary to move a straight edge dislocation has the form $\tau_p = \frac{2G_m}{(1-\nu)} \exp\left(\frac{-2\pi w}{b}\right)$, where G_m is the shear modulus, ν is the Poisson's ratio, and w is the defect core width. Thus, wide core width and small magnitude of Burgers vector lead to mobile defects. Attendant shuffling reduces the disconnection mobility [27]: shuffling is defined here as any additional atomic displacements necessary to restore perfect twin crystal structure beyond the displacement of each atom by \boldsymbol{b} when a disconnection moves along the boundary [54]. Since small step height, h, is thought to promote both wide cores and simple shuffles [27,80], it is used here as a guide to mobility.

To illustrate the comparison of $type\ I$ and $type\ II$ twins in NMG, we choose a non-conjugate pair of incompatible twins which has been observed in several experimental investigations [19,61,62]. The K_1 planes of these two twins, $(0\overline{1}1)_m$ and $(q_1\overline{1}1)_m$, have very similar orientations, as depicted schematically in Figure 8: thus their traces on a $(100)_m$ surface differ by only about 6° [19,61,62]. Inspection of Table 1 and Figure 3 shows that a $(0\overline{1}1)_m$ twin is related to the conjugate of the $(q_1\overline{1}1)_m$ twin, i.e. the $(011)_m$ twin, by the $(001)_m$ crystal mirror plane. The early stage of growth of the $(0\overline{1}1)_m$ twin is depicted schematically in Figure 3 (b), and formation of the $(q_1\overline{1}1)_m$ twin from its $(011)_m$ precursor is shown in Figure 4. As the twin grows, the area of the TB increases until the twin transects the entire specimen: we refer to this position, where the area of TB has reached maximum, as the reference location, as shown in Figure 8 for $type\ I$ (a) and $type\ II$ (b) twins.

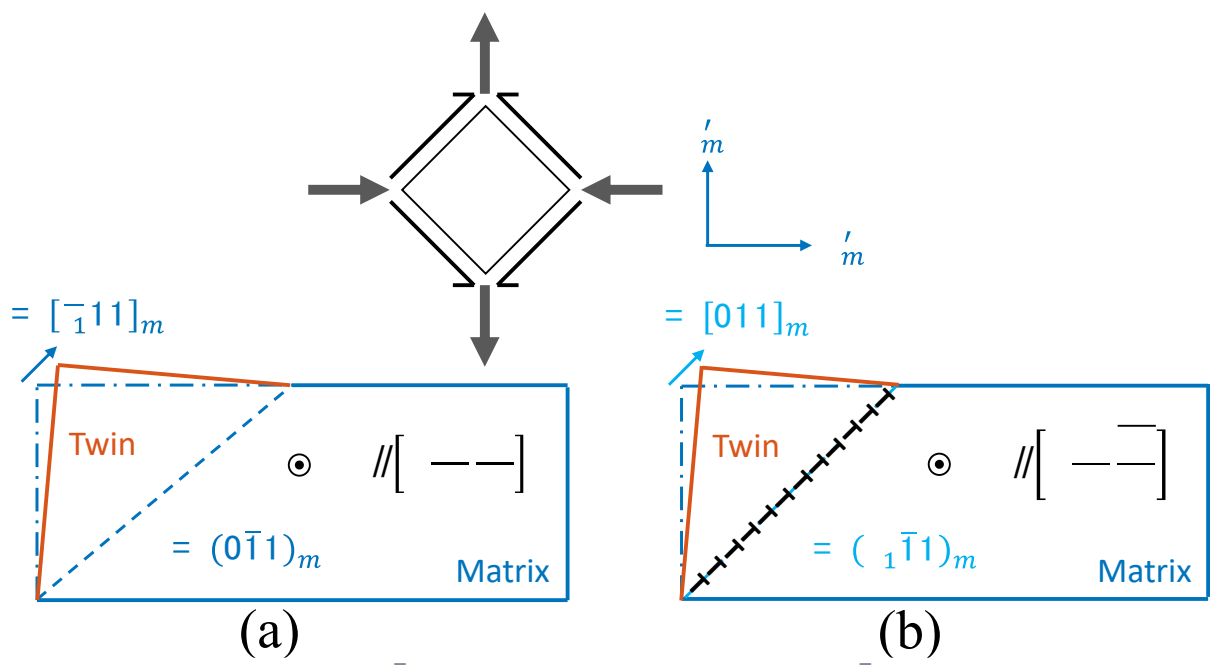


Figure 8: Schematic illustration of (a) $(0\bar{1}1)_m$ type I twin boundary (TB) and (b) $(q_1\bar{1}1)_m$ type II TB in the reference location. The k_1 , γ_1 in (a) and k_2 , γ_2 in (b) are <u>not</u> a conjugate pair.

5.2 MOBILITY OF TYPE I TWINS

In a $(0\bar{1}1)_m$ type I twin, glissile disconnections with smallest magnitude Burgers vector have $|\boldsymbol{b}|=0.0259$ nm with a corresponding high \dot{N} at ambient temperature. At equilibrium, the type I TB at the reference location is flat with no disconnections present: it is anticipated that the interface structure is sharp and of relatively low energy. In response to a driving force, nucleation and propagation of disconnections along the rational TB produce the engineering shear $\gamma_e=|\boldsymbol{b}|/h=0.1274$, where $h=d_{(0\bar{2}2)_m}=0.2035$ nm. Since \boldsymbol{b} is parallel to $\boldsymbol{\eta}_1=[\bar{r}_111]_m$, these defects have pure edge character if their line direction, $\boldsymbol{\xi}$, is parallel to $\boldsymbol{n}_s=[1\ q_1/2\ q_1/2]_m$. Since the line direction is irrational, these defects may lie predominantly along $[100]_m$ Peierls valleys for minimum energy, with kinks spaced approximately every $10\ a_m$, as discussed in Section 4.3. The core width, w, is best investigated using computer simulations, but limited results have been published for defects in NMG. Nonetheless, simulations of disconnections for compound twins in hcp metals indicate that the cores of disconnections with small h can be relatively wide [81–83].

The disconnection motion described above is conservative, i.e. no climb is involved, because \boldsymbol{b} is parallel to the $(0\overline{1}1)_m$ twin plane. Moreover, shuffling accompanying the defect motion is expected to be small: in austenitic NMG, all four atoms in the basis lie in the $(0\overline{1}1)_c$ plane, and since the martensite is a slight monoclinic distortion of the cubic phase, all four atoms in the basis are expected to remain close to the $(0\overline{1}1)_m$ plane. Thus, all atoms are displaced by \boldsymbol{b} as a disconnection sweeps along the boundary, and minimal additional shuffles are anticipated.

Taking all the factors mentioned above into account, we anticipate relatively easy motion of disconnections in $type\ I$ twins because \dot{N} and \dot{G} are significant. For modest driving forces, kink motion along the disconnections, rather than rigid disconnection motion, may be the elemental mechanism of twin growth: quantitative assessment of the energy barrier opposing the motion is beyond the scope of the paper. Furthermore, we surmise that TB mobility is temperature dependent because the activation energy for disconnection motion in a periodic rational interface, either by rigid disconnection motion or kink motion, is assisted by thermal energy.

It has also been reported that the twinning stress is a function of imposed strain rate [72,84,85], and this has been ascribed to increased viscous drag at higher velocities. This behavior may arise in part from increased damping at higher disconnection velocities, analogous to that of dislocation velocity as a function of applied stress in single crystals [79], but additional dissipative mechanisms, such as magnetization rotation and domain wall motion, are also likely to be active in NMG, and are not considered further here.

5.3 MOBILITY OF *TYPE II* TWINS

The formation of a $(q_1\overline{1}1)_m$ type II TB according to the TM, is depicted schematically in Figure 4. Disconnection half-loops with ${\bf b}$ parallel to $[r_1\overline{1}1]_m$ are initially nucleated at the surface source and glide on the $(011)_m$ plane forming a nascent type I twin. However, their progress is impeded, as described in **Section 3.2**, so they accumulate into a wall of edge defects approximately perpendicular to $(011)_m$. The displacement field of these defects, with line direction ${\bf \xi}$ parallel to ${\bf n}_s = \left[1\,q_1/2\,\overline{q_1/2}\right]_m$, exhibits both strain and rotational distortion. The latter sums to a rigid body rotation equal to $2\alpha = 7.29^\circ$ between the matrix and twin. This rotational relaxation is unconstrained in the present case since the twin crystal has free surfaces.

5.3.1 Sharp $(q_1\overline{1}1)_m$ type II twins

Figure 8 (b) schematically illustrates the structure of this sharp $(q_1\overline{1}1)_m$ type II twin in the reference location when viewed along \textbf{n}_s . Disconnections can be introduced into this boundary, as outlined in **Section 4.2** and illustrated schematically in Figure 5 (b): those with the smallest Burgers vector and step height are formed using $\textbf{t}(\lambda) = \frac{1}{2}[110]_m$ and $\textbf{t}(\mu) = \frac{1}{2}[\overline{1}01]_m$ in Equations (1) and (2), and P corresponds to the 2' axis parallel to $\textbf{\eta}_1 = [011]_m$. The resulting b is parallel to $\textbf{\eta}_1$ with magnitude 0.0231 nm, and h = 0.1815 nm. The result is consistent with previous modeling in terms of an offset tilt wall [70], as illustrated schematically in Figure 5 (b), and $\gamma_e = 0.1274$, identical to that of the $type\ I$ conjugate twin. Thus, glissile disconnections could either be nucleated as half-loops at the surface or homogeneously on the boundary as complete loops. In either case, \dot{N} , is expected to be similar to that of $type\ I$ twins at ambient temperature.

As depicted in Figure 4, the defects in the $type\ II$ TB can be regarded either as disconnections with characteristic topological parameters (\boldsymbol{b},h) , or as offsets in the tilt wall [70]. In the latter visualization, $type\ I$ disconnections initially glide on the $(011)_m$ planes, and form tilt walls in the manner described by Read and Shockley [86]. In this configuration, the disconnections lose their step character, becoming grain boundary dislocations with residual Burgers vector, \boldsymbol{b}^g , perpendicular to the interface. Thus, lateral motion of $type\ II$ disconnections, (\boldsymbol{b},h) , can alternatively be regarded as motion of the grain boundary dislocations in the direction normal to the interface. Dynamic simulations are needed to elucidate the extent of shuffling in the present case. Nonetheless, as has been described in **Section 5.2**, shuffling is thought to be minimal for such motion.

Unlike type I boundaries considered previously, these type II disconnections are superimposed on a high energy TB, with only one rational direction, η_1 , in the twin plane. Therefore, deep Peierls valleys can only be envisaged lying along this direction. Thus, disconnections with line direction other than η_1 are likely to have delocalized cores. Consequently, we expect $\sigma_{II}^t(T)$ to be lower than $\sigma_I^t(T)$. Moreover, if the activation energy for disconnection motion is comparable to thermal energy, $\sigma_{II}^t(T)$ would be effectively temperature independent, as is observed experimentally [61,87].

5.3.2 Ragged $(q_1\overline{1}1)_m$ type II twins

In this model, the *type I* disconnections that accumulate in the tilt wall are kinked on their rational $(011)_m$ glide planes. The line direction, $\xi \parallel \begin{bmatrix} 1 \ 0.0529 \ \overline{0.0529} \end{bmatrix}_m$ in the sharp interface can be approximated as $\approx 10[100]_m + 1/2[01\overline{1}]_m$. In other words, a disconnection lies along a $[100]_m$ Peierls valley with kinks spaced about every $10a_m$, as depicted schematically in Figure 6. In the most orderly arrangement, the kinks on the successive $(011)_m$ planes are vertically aligned (Figure 6 (b)), and increasingly disordered configurations can be imagined (Figure 6 (c)).

As discussed in **Section 5.3.1**, the migration of ragged *type II* TBs can be regarded either in terms of *type II* disconnections (\boldsymbol{b},h) , or forward motion of the now kinked grain boundary dislocations in offset tilt walls. One consequence of the boundary becoming less sharp is that the effective width, w, of *type II* disconnections increases, thereby tending to lower $\sigma_{II}^t(T)$ and reducing the activation barrier for defect motion.

5.3.3 Coherently faceted type II twin approximants

In **Section 4.2** the concept of a (*misfit-relieved*) coherent (*low-index*) approximant to a type II twin was introduced. In this relaxation mechanism, the sharp type II TB maximizes the extent of coherent $(0\overline{1}1)_m$ interface. In the reference location, this interface structure would differ from that of the $(0\overline{1}1)_m$ type I twin discussed in **Section 5.2**. While the latter is flat with no disconnections present, the former is reticulated by an array of screw disconnections to

accommodate the shear coherency strain. We assume that the coherency strain appears spontaneously, and that the screw disconnections with ${m b}^m \parallel [0\bar{1}\bar{1}]_m$ are nucleated at the surface sources. As shown in Appendix C, the final interface orientation of the coherent approximant TB rotates away from $(q_1\bar{1}1)_m$. Under the influence of a driving force, the disconnections in the array move synchronously perpendicular to their line direction thereby producing an engineering shear. Since the overall orientation relationship between the crystals has not changed, the smallest magnitude Burgers vector, given in Table 2 for the $(q_1\bar{1}1)_m$ twin, is enhanced by the coherency strain, giving $|{m b}^m|=0.0233$ nm. Similarly, $h=d_{(0\bar{2}2)_m}=0.2035$ nm, resulting in $\gamma_e=0.1147$. If the coherency strain is assumed to be partitioned equally between the crystals, the rational vectors $[100]_m$ and $[01\bar{1}]_m$ in the $(0\bar{1}1)_m$ interface become orthogonal, thus resembling a compound twin structure near the interface. Defect motion would therefore need to be activated thermally to surmount the Peierls barriers. Consequently, we expect $\sigma_{II}^t(T)$ to be higher than for the ragged structure. Further, $\sigma_{II}^t(T)$ of the coherent approximant would be temperature dependent.

6 CONCLUSIONS

The objective of the present work is to elucidate the exceptional mobility of *type II* twins in NMG. Their structure has been investigated through the TM [38], with particular emphasis on the role of disconnections in determining the twinning stress and its temperature dependence, $\sigma_{II}^t(T)$. Our principal conclusions are as follows.

A type II twin can form by surface nucleation of a precursor twin, which is its type I conjugate, as in the model of Pond and Hirth [38]. An applied stress leads to nucleation of disconnections in the precursor k_1 plane, which due to lack of mobility, accumulate and form a tilt wall; after symmetric partitioning of the rotational distortions, the boundary exhibits the crystallography of the k_2 twin predicted by the CM [22,27]. The defects forming this wall may form (i) a "sharp" array of aligned edge dislocations, or (ii) a more "ragged" configuration by virtue of individual defects becoming kinked in their k_1 plane, and/or progressive misalignment of defects within the array, or (iii) a misfit-relieved coherently faceted interface.

Sharp $type\ II$ twins can host glissile disconnections with high mobility, leading to fast interface migration. It is suggested that this arises because such disconnections have wider cores than their counterparts in $type\ I$ twins, combined with simple shuffles accompanying their motion. Ancillary consequences are that the magnitude and temperature dependence of $\sigma_{II}^t(T)$ for $type\ II$ twins are expected to be lower than those quantities for $type\ I$ twins, $\sigma_I^t(T)$. For ragged $type\ II$ twins, we anticipate this trend to be more pronounced because of the increase in effective core width.

Previous authors have suggested that a $type\ II$ twin may lower its interfacial energy by reconfiguring into a misfit-relieved assembly of coherent low-index facets [30,57-60]. Here, we considered such a mechanism for $(q_1\overline{1}1)_m$ $type\ II$ twins by formation of $(0\overline{1}1)_m$ facets. We assume the $(0\overline{1}1)_m$ facets spontaneously adopt a 2-D periodic structure through a coherency strain of less than 1%, and this displacement field is accommodated by an array of superimposed screw disconnections. However, according to the TM, the step sense of disconnections with the appropriate sense of Burgers vector leads to the misfit-relieved interface that rotates away from $(q_1\overline{1}1)_m$ rather than towards it, contrary to experimental observations. Thus, we find that surface nucleated $(q_1\overline{1}1)_m$ $type\ II$ twins in NMG are unlikely to adopt a facetted configuration. This conclusion is consistent with the expectation that such structures would exhibit higher magnitudes of $\sigma_{II}^t(T)$ and lower mobilities because the admissible disconnections would have relatively narrower cores.

APPENDICES

APPENDIX A: TRANSFORMATION MATRICES

Let α and β designate alternative unit cell representations of the same crystal. Then reciprocal space vectors transform co-variantly and real space vectors transform contra-variantly [88]:

$$(h k l)_{\alpha} = (h' k' l')_{\beta \beta} \mathbf{P}_{\alpha} \tag{A1}$$

$$\begin{pmatrix} u \\ v \\ w \end{pmatrix}_{\alpha} = {}_{\alpha} \mathbf{P}_{\beta} \begin{pmatrix} u' \\ v' \\ w' \end{pmatrix}_{\beta} \tag{A2}$$

where, $_{\alpha}\boldsymbol{P}_{\beta}=_{\beta}\boldsymbol{P}_{\alpha}^{-1}.$

From the electron diffraction pattern shown in Figure 1 (c), we observe, $(0\ 0\ 10)_{10M} \rightarrow (\overline{220})_m$, $(\overline{200})_{10M} \rightarrow (\overline{220})_m$ and $(020)_{10M} \rightarrow (002)_m$. Thus, we calculate the transformation matrices as follows:

$${}_{10M}\boldsymbol{P}_{m} = \frac{1}{5} \begin{pmatrix} 5 & -5 & 0 \\ 0 & 0 & 5 \\ -1 & -1 & 0 \end{pmatrix} \tag{A3}$$

$$_{m}\boldsymbol{P}_{10M} = \frac{1}{2} \begin{pmatrix} 1 & 0 & -5 \\ -1 & 0 & -5 \\ 0 & 2 & 0 \end{pmatrix} \tag{A4}$$

APPENDIX B: BEVIS & CROCKER THEORY

A homogeneous simple shear is represented by an affine transformation as:

$$v = S \cdot u \tag{B1}$$

where u and v are lattice vectors of the parent and twin respectively, and s is a second rank tensor defining the shear transformation. In some general coordinate system s, the equation s is a second rank tensor defining the shear transformation. In some general coordinate system s, the equation s is a second rank tensor defining the shear transformation convention as:

$${}^{A}v^{i} = {}^{A}S^{i}_{i} \cdot {}^{A}u^{j} \tag{B2}$$

In the general coordinate system A, ${}^{A}S_{i}^{i}$, has the form:

$${}^{A}S_{i}^{i} = \delta_{i}^{i} + s \cdot {}^{A}l^{i} \cdot {}^{A}m_{j} \tag{B3}$$

where δ_j^i is the Kronecker delta, \boldsymbol{l} is the unit vector parallel to the shear direction, \boldsymbol{m} is the unit vector normal to the invariant plane and s is the twinning shear. In general, equation B2 yields irrational components for ${}^A\boldsymbol{v}$. However, \boldsymbol{v} is a lattice vector of the twin in a new coordinate system B, where B is related to A by some rotation or reflection, \boldsymbol{L} . So,

$${}^{B}\boldsymbol{v} = \boldsymbol{L} \cdot {}^{A}\boldsymbol{S} \cdot {}^{A}\boldsymbol{u} = \boldsymbol{C} \cdot {}^{A}\boldsymbol{u} \tag{B4}$$

where \boldsymbol{C} is the unimodular correspondence matrix.

Once the correspondence matrix, C, is specified, Bevis and Crocker [22] showed that we can utilize its properties to calculate s, l and m. Using matrix notation, the solutions for s, l and m are found as follows:

$$s = \operatorname{trace}(\mathbf{C}' \cdot \mathbf{G} \cdot \mathbf{C} \cdot \mathbf{G}^{-1}) - 3 \tag{B5}$$

where,

$$\mathbf{G} = \begin{pmatrix} \mathbf{a} \cdot \mathbf{a} & \mathbf{a} \cdot \mathbf{b} & \mathbf{a} \cdot \mathbf{c} \\ \mathbf{b} \cdot \mathbf{a} & \mathbf{b} \cdot \mathbf{b} & \mathbf{b} \cdot \mathbf{c} \\ \mathbf{c} \cdot \mathbf{a} & \mathbf{c} \cdot \mathbf{b} & \mathbf{c} \cdot \mathbf{c} \end{pmatrix} = \begin{pmatrix} a_m^2 & a_m b_m \cos \gamma & 0 \\ a_m b_m \cos \gamma & b_m^2 & 0 \\ 0 & 0 & c_m^2 \end{pmatrix}$$
(B6)

is the metric tensor for the present case. Using $Y = G - C' \cdot G \cdot C$, we obtain three quadratic equations, defined by the equation:

$$Y_{ii} \cdot m_i^2 - 2Y_{ij} \cdot m_i \cdot m_j + Y_{ij} \cdot m_i^2 = 0$$
 (B7)

where $i \neq j$, and i, j = 1, 2, 3. Equation B7 yields two possible solutions for m, which are the conjugate undistorted planes k_1 and k_2 . l can then be obtained directly from equation B3, or derived from Y^{-1} using three quadratic equations like B7. Yet again, we obtain two solutions for l, which are the conjugate shear directions γ_1 and γ_2 .

In the case of twinning, equation B4 shows that a correspondence matrix for a conventional twin can be formulated as a $\mathbf{2}'$ operation. Thus, the complete set of correspondence matrices

for conventional twins is isomorphous with the 2-fold symmetry operations which were present in the austenite, but which are suppressed by the monoclinic distortion. There are 12 such operations in the present case, but, in the light of equation B7 which shows that there are two solutions, k_1 and k_2 , for each choice of C, we may select just 6 of these. Furthermore, it is helpful to subdivide these 6 into the operations which leave the $(001)_m$ crystal mirror plane invariant, i.e. $\mathbf{2}'_{[100]_c}$ and $\mathbf{2}'_{[110]_c}$, because these lead to compound twins, and the others, $\mathbf{2}'_{[101]_c}$, $\mathbf{2}'_{[101]_c}$, $\mathbf{2}'_{[011]_c}$ and $\mathbf{2}'_{[011]_c}$, which lead to $type\ I-type\ II$ pairs. The C matrix for each of these operations is listed in Table B1.

Table B1: Correspondence matrices formulated as 2' symmetry operations that are suppressed in the martensite phase compared to its austenite parent phase.

Compound twins			Type I and type II twins				
	$2'_{[100]_c}$	$2'_{[110]_c}$	$2'_{[011]_c}$	$2_{[0\overline{1}1]_{c}}^{\prime}$	$2'_{[101]_c}$	$\mathbf{2'_{[\overline{1}01]_c}}$	
С	$\begin{bmatrix} 1 & 0 & 0 \\ 0 & -1 & 0 \\ 0 & 0 & -1 \end{bmatrix}$	$\begin{bmatrix} 0 & 1 & 0 \\ 1 & 0 & 0 \\ 0 & 0 & -1 \end{bmatrix}$	$\begin{bmatrix} -1 & 0 & 0 \\ 0 & 0 & 1 \\ 0 & 1 & 0 \end{bmatrix}$	$\begin{bmatrix} -1 & 0 & 0 \\ 0 & 0 & -1 \\ 0 & -1 & 0 \end{bmatrix}$	$\begin{bmatrix} 0 & 0 & 1 \\ 0 & -1 & 0 \\ 1 & 0 & 0 \end{bmatrix}$	$ \begin{bmatrix} 0 & 0 & -1 \\ 0 & -1 & 0 \\ -1 & 0 & 0 \end{bmatrix} $	

APPENDIX C: COHERENTLY FACETED APPROXIMANT TO TYPE II INTERFACE

It is possible that the energy of a *type II* TB can be reduced by the formation of coherent facets: for example, recent work by Mohammed and Sehitoglu [60] used atomic-scale simulation to investigate a faceted approximant structure in NiTi. Since the boundary plane of a *type II* twin is an invariant plane, there is no long-range elastic strain field. If the boundary reconfigures to become faceted, any coherency strain at these facets (or terraces) would have to be accommodated by the introduction of an array of appropriate interfacial defects. If these defects are disconnections, their step character would cause the overall interface orientation to rotate away from the facet orientation. In an ideal approximant structure, the array of misfit-removing defects would not only fully accommodate any coherency strain but also rotate the interface orientation to that of the *type II* twin. Here, we consider the $(q_1\bar{1}1)_m$ type II twin in NMG.

The axis/angle pair defining the orientation relationship between the two crystals in the approximant configuration is taken to be the same as that for the $type\ II$ twin, i.e. $P(II) = [011]_m/\pi$, so all planes in the $[011]_m$ zone are common to both crystals. However, these planes are not coherent in 2-D, i.e. $[011]_m$ is the only coincident rational direction in these planes. We focus on the $(0\bar{1}1)_m$ plane, which is inclined by only 4.12° to $(q_1\bar{1}1)_m$. As illustrated in Figure 7, this plane becomes coherent in 2-D by the imposition of a small coherency shear strain parallel to $[011]_m$. Such a coherency strain can be accommodated by a superimposed array of screw disconnections, and, since these defects have step character, the

average interface plane consequently rotates away from the $(0\bar{1}1)_m$ "terrace" orientation. We investigate whether the misfit can be fully relieved in this manner, and whether the interface structure rotates to an orientation close to the $(q_1\bar{1}1)_m$ plane. Since $(0\bar{1}1)_m$ type I TBs are observed experimentally in NMG [19,61,62], implying that they have low interfacial energy, this stepped configuration with $(0\bar{1}1)_m$ terraces might be energetically feasible. In the coherently strained $(0\bar{1}1)_m$ terrace illustrated in Figure 7 (b), the $[100]_m$ and $[011]_m$ directions become orthogonal, whereas they are not so in a $(0\bar{1}1)_m$ type I interface.

We imagine the creation of a bicrystal with a 2-D coherent $(0\bar{1}1)_m$ planar interface by the application of shear tractions to the external (top and bottom) surfaces: these tractions produce homogenous strains which are equally partitioned between the two crystals. Thus, the directions $[100]_m^\mu$ and $[\bar{1}00]_m^\lambda$, which were originally inclined by 0.53° , are brought into parallelism, and become perpendicular to the common $[011]_m$ axis. The defect content of the 2-D coherent interface can be established by applying the Frank-Bilby [89] equation. We introduce a coordinate frame where the coherent $(0\bar{1}1)_m$ terrace plane has embedded interface coordinates x, y, z with $x \parallel [011]_m$ and z parallel to the interface normal. Following Hirth et al. [89], we define the matrix, D_{ij} , which quantifies the elastic distortions required to transform the "natural" bicrystal into the "sheared-coherent" form: the only non-zero element is $D_{12} = -2 \cdot \tan(0.53^\circ/2) = -0.0092$. When this matrix operates on a probe vector, v, we obtain the coherency dislocation content, b^c , necessary to sustain coherency. Using $v = [0, -v_y, 0]$ (for consistency with the RH/FS convention [79]), we obtain $b^c = [-D_{12}v_y, 0, 0]$. Thus, b^c is parallel to x, so these dislocations have RH screw character.

To compensate for the resulting displacement field, we introduce an array of equally spaced LH screw disconnections (\boldsymbol{b}^m,h^m) in the interface, where $\boldsymbol{b}^m=P(II)^{-1}\boldsymbol{t}^c(\lambda)-\boldsymbol{t}^c(\mu)$, and $h^m=\boldsymbol{n}\cdot\boldsymbol{t}^c(\mu)=\boldsymbol{n}\cdot P(II)^{-1}\boldsymbol{t}^c(\lambda)$: here, $\boldsymbol{t}^c(\mu)$ and $\boldsymbol{t}^c(\lambda)$ are translation vectors in the coherent dichromatic pattern (CDP), and \boldsymbol{n} is the unit normal to the $(0\bar{1}1)_m$ plane (i.e. the same as \boldsymbol{m} in equation B7). For the smallest magnitude $|\boldsymbol{b}^m|$, we use $\boldsymbol{t}^c(\mu)=1/2[10\bar{1}]_m$ and $\boldsymbol{t}^c(\lambda)=1/2[\bar{1}10]_m$, i.e. rational vectors with opposite sense of those shown in Table 2 for disconnections in the $(q_1\bar{1}1)_m$ twin. These translation vectors give us $\boldsymbol{b}^m\parallel[0\bar{1}1]_m$. The coherency strain enhances the magnitude of the Burgers vector by $(1+|D_{12}|)$ compared with the value given in Table 2 for the $type\ II$ twin, giving $|\boldsymbol{b}^m|=0.0233$ nm, and the defects' step height is $h^m=d_{(0\bar{2}2)_m}=0.2035$ nm.

This disconnection array is shown schematically in Figure C1. We define a second interfacial coordinate frame x', y', z', inclined to the terrace by angle θ . In the terrace frame, the Burgers vector can be written as $\boldsymbol{b}^m = [-b_x^m \ 0 \ 0]$, and remains the same when resolved into the inclined interface frame. The distortion matrix transformed into the inclined frame has non-

zero components $D_{12}' = D_{12}\cos\theta$, and $D_{13}' = -D_{12}\sin\theta$. Thus, for misfit relief on that plane, i.e. $\mathbf{B} = -\mathbf{b}^c$, and putting $v_y = L$, where L is the disconnection spacing on this plane, we have $L \cdot D_{12}\cos\theta = b_x^m$. Since $\sin\theta = h^m/L$, we have $\tan\theta = h^m \cdot D_{12}/b_x^m$, and hence $\theta = 4.59^\circ$ in the present case. The residual strain, $D_{13}' < 0.1\%$, cannot be compensated by any regular defect array in the x'y' plane. Thus, for NMG, the partially misfit-relieved faceted coherent plane would be inclined at $4.12^\circ + 4.59^\circ = 8.71^\circ$, i.e. it rotates away from the invariant $(q_1\overline{1}1)_m$ plane, as shown in Figure C1.

Referring to Figure C1, we can determine whether the stress indicated in Figure 4 would grow or diminish the twin crystal. In the present case, the applied shear causes the disconnections in the array to move leftwards thereby promoting twin growth. The resulting engineering strain would have magnitude 0.1147.

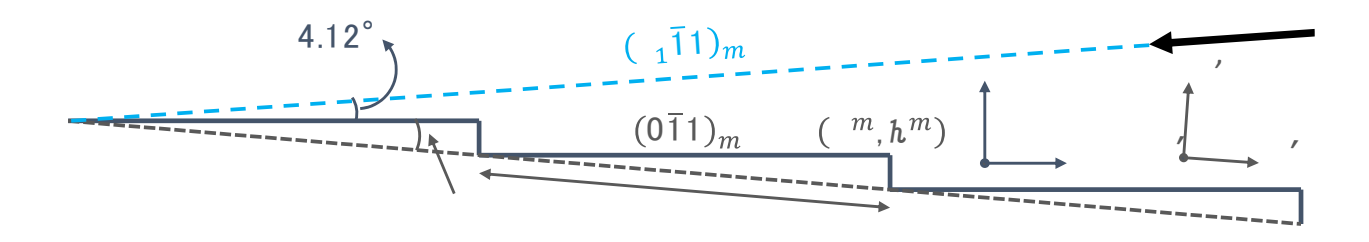


Figure C1: Schematic illustration of misfit accommodation at a coherently faceted approximant structure. The line direction of RH coherency dislocations, $\boldsymbol{\xi}^c$, pointing out of the page, is parallel to $[011]_m$. The angle between $(0\bar{1}1)_m$ and $(q_1\bar{1}1)_m$ is 4.12° . The LH screw misfit disconnections have \boldsymbol{b}^m anti-parallel to $\boldsymbol{\xi}^c$ and a negative sense of steps. The direction \boldsymbol{n}_s is the average line direction of the twinning disconnections in the $(q_1\bar{1}1)_m$ twin plane.

REFERENCESA

- [1] S.J. Murray, M. Marioni, S.M. Allen, R.C. O'Handley, T.A. Lograsso, 6% magnetic-field-induced strain by twin-boundary motion in ferromagnetic Ni–Mn–Ga, Appl. Phys. Lett. 77 (2000) 886–888. https://doi.org/10.1063/1.1306635.
- [2] A. Sozinov, A.A. Likhachev, K. Ullakko, Crystal structures and magnetic anisotropy properties of Ni-Mn-Ga martensitic phases with giant magnetic-field-induced strain, IEEE Trans. Magn. 38 (2002) 2814–2816. https://doi.org/10.1109/tmag.2002.803567.
- [3] D. Kellis, A. Smith, K. Ullakko, P. Müllner, Oriented single crystals of Ni–Mn–Ga with very low switching field, J. Cryst. Growth. 359 (2012) 64–68. https://doi.org/10.1016/j.jcrysgro.2012.08.014.
- [4] M.A. Marioni, R.C. O'Handley, S.M. Allen, Pulsed magnetic field-induced actuation of Ni–Mn–Ga single crystals, Appl. Phys. Lett. 83 (2003) 3966–3968. https://doi.org/10.1063/1.1626021.
- [5] I. Suorsa, E. Pagounis, K. Ullakko, Magnetic shape memory actuator performance, J. Magn. Magn. Mater. 272–276 (2004) 2029–2030. https://doi.org/10.1016/j.jmmm.2003.12.1026.

- [6] A.R. Smith, J. Tellinen, K. Ullakko, Rapid actuation and response of Ni–Mn–Ga to magnetic-field-induced stress, Acta Mater. 80 (2014) 373–379. https://doi.org/10.1016/j.actamat.2014.06.054.
- [7] S.A. Wilson, R.P.J. Jourdain, Q. Zhang, R.A. Dorey, C.R. Bowen, M. Willander, Q.U. Wahab, M. Willander, S.M. Al-Hilli, O. Nur, E. Quandt, C. Johansson, E. Pagounis, M. Kohl, J. Matovic, B. Samel, W. Van Der Wijngaart, E.W.H. Jager, D. Carlsson, Z. Djinovic, M. Wegener, C. Moldovan, R. Iosub, E. Abad, M. Wendlandt, C. Rusu, K. Persson, New materials for microscale sensors and actuators, Mater. Sci. Eng. R Rep. 56 (2007) 1–129. https://doi.org/10.1016/j.mser.2007.03.001.
- [8] P. Lindquist, T. Hobza, C. Patrick, P. Müllner, Efficiency of Energy Harvesting in Ni–Mn–Ga Shape Memory Alloys, Shape Mem. Superelasticity. 4 (2018) 93–101. https://doi.org/10.1007/s40830-018-0158-z.
- [9] S. Barker, E. Rhoads, P. Lindquist, M. Vreugdenhil, P. Müllner, Magnetic Shape Memory Micropump for Submicroliter Intracranial Drug Delivery in Rats, J. Med. Devices. 10 (2016) 041009. https://doi.org/10.1115/1.4034576.
- [10] K. Ullakko, L. Wendell, A. Smith, P. Müllner, G. Hampikian, A magnetic shape memory micropump: contact-free, and compatible with PCR and human DNA profiling, Smart Mater. Struct. 21 (2012) 115020. https://doi.org/10.1088/0964-1726/21/11/115020.
- [11] I. Aaltio, K.P. Mohanchandra, O. Heczko, M. Lahelin, Y. Ge, G.P. Carman, O. Söderberg, B. Löfgren, J. Seppälä, S.-P. Hannula, Temperature dependence of mechanical damping in Ni–Mn–Ga austenite and non-modulated martensite, Scr. Mater. 59 (2008) 550–553. https://doi.org/10.1016/j.scriptamat.2008.05.005.
- [12] J. Pons, R. Santamarta, V.A. Chernenko, E. Cesari, Structure of the layered martensitic phases of Ni–Mn–Ga alloys, Mater. Sci. Eng. A. 438–440 (2006) 931–934. https://doi.org/10.1016/j.msea.2006.02.179.
- [13] L. Straka, O. Heczko, H. Seiner, N. Lanska, J. Drahokoupil, A. Soroka, S. Fähler, H. Hänninen, A. Sozinov, Highly mobile twinned interface in 10M modulated Ni–Mn–Ga martensite: analysis beyond the tetragonal approximation of lattice, Acta Mater. 59 (2011) 7450–7463. https://doi.org/10.1016/j.actamat.2011.09.020.
- [14] R. Chulist, E. Pagounis, A. Böhm, C.-G. Oertel, W. Skrotzki, Twin boundaries in trained 10M Ni–Mn–Ga single crystals, Scr. Mater. 67 (2012) 364–367. https://doi.org/10.1016/j.scriptamat.2012.05.026.
- [15] A. Sozinov, N. Lanska, A. Soroka, L. Straka, Highly mobile type II twin boundary in Ni-Mn-Ga five-layered martensite, Appl. Phys. Lett. 99 (2011) 124103. https://doi.org/10.1063/1.3640489.
- [16] R. Chulist, L. Straka, N. Lanska, A. Soroka, A. Sozinov, W. Skrotzki, Characterization of mobile type I and type II twin boundaries in 10M modulated Ni–Mn–Ga martensite by electron backscatter diffraction, Acta Mater. 61 (2013) 1913–1920. https://doi.org/10.1016/j.actamat.2012.12.012.
- [17] R. Abeyaratne, S. Vedantam, A lattice-based model of the kinetics of twin boundary motion, J. Mech. Phys. Solids. 51 (2003) 1675–1700. https://doi.org/10.1016/s0022-5096(03)00069-3.
- [18] E. Faran, D. Shilo, The kinetic relation for twin wall motion in Ni-Mn-Ga, J. Mech. Phys. Solids. 59 (2011) 975–987. https://doi.org/10.1016/j.jmps.2011.02.009.

- [19] E. Faran, D. Shilo, The kinetic relation for twin wall motion in Ni-Mn-Ga—part 2, J. Mech. Phys. Solids. 61 (2013) 726–741. https://doi.org/10.1016/j.jmps.2012.11.004.
- [20] H. Seiner, L. Straka, O. Heczko, A microstructural model of motion of macro-twin interfaces in Ni–Mn–Ga 10M martensite, J. Mech. Phys. Solids. 64 (2014) 198–211. https://doi.org/10.1016/j.jmps.2013.11.004.
- [21] J. Wang, P. Du, Theoretical study and numerical simulations on the stress-induced twin interface nucleation in single-crystalline Ni-Mn-Ga alloys, J. Appl. Phys. 126 (2019) 115101. https://doi.org/10.1063/1.5115486.
- [22] M. Bevis, A.G. Crocker, Twinning shears in lattices, Proc. R. Soc. Lond. Ser. Math. Phys. Sci. 304 (1968) 123–134. https://doi.org/10.1098/rspa.1968.0077.
- [23] R.W. Cahn, Plastic deformation of alpha-uranium; twinning and slip, Acta Metall. 1 (1953) 49–70. https://doi.org/10.1016/0001-6160(53)90009-1.
- [24] F.C. Frank, A note on twinning in alpha-uranium, Acta Metall. 1 (1953) 71–74. https://doi.org/10.1016/0001-6160(53)90010-8.
- [25] M.A. Jaswon, D.B. Dove, The crystallography of deformation twinning, Acta Crystallogr. 13 (1960) 232–240. https://doi.org/10.1107/S0365110X60000534.
- [26] B.A. Bilby, A.G. Crocker, The theory of the crystallography of deformation twinning, Proc. R. Soc. Lond. Ser. Math. Phys. Sci. 288 (1965) 240–255. https://doi.org/10.1098/rspa.1965.0216.
- [27] J.W. Christian, S. Mahajan, Deformation twinning, Prog. Mater. Sci. 39 (1995) 1–157.
- [28] K. Bhattacharya, Theory of Martensitic Microstructure and the Shape-Memory Effect, in: Microstruct. Martensite, 2004: p. 87.
- [29] M. Bevis, A.G. Crocker, Twinning modes in lattices, Proc. R. Soc. Math. Phys. Eng. Sci. 313 (1969) 21. https://doi.org/10.1098/rspa.1969.0208.
- [30] K.M. Knowles, A high-resolution electron microscope study of nickel-titanium martensite, Philos. Mag. A. 45 (1982) 357–370. https://doi.org/10.1080/01418618208236176.
- [31] M. Nishida, K. Yamauchi, I. Itai, H. Ohgi, A. Chiba, High resolution electron microscopy studies of twin boundary structures in B19' martensite in the Ti-Ni shape memory alloy, Acta Metall. Mater. 43 (1995) 1229–1234. https://doi.org/10.1016/0956-7151(94)00328-f.
- [32] R.C. Pond, S. Celotto, Special interfaces: military transformations, Int. Mater. Rev. 48 (2003) 225–245. https://doi.org/10.1179/095066003225010245.
- [33] P. Komninou, E. Polychroniadis, J.G. Antonopoulos, T. Karakostas, P. Delavignette, A DISLOCATION MECHANISM FOR THE GROWTH OF TWINS IN DEFORMED HCP METALS, J. Phys. Colloq. 51 (1990) C1-C1-219. https://doi.org/10.1051/jphyscol:1990133.
- [34] S. Kustov, A. Saren, A. Sozinov, V. Kaminskii, K. Ullakko, Ultrahigh damping and Young's modulus softening due to a/b twins in 10M Ni-Mn-Ga martensite, Scr. Mater. 178 (2020) 483–488. https://doi.org/10.1016/j.scriptamat.2019.12.024.
- [35] R.C. Pond, D.J. Bacon, A. Serra, A.P. Sutton, The crystallography and atomic structure of line defects in twin boundaries in hexagonal-close-packed metals, Metall. Trans. A. 22 (1991) 1185–1196. https://doi.org/10.1007/BF02660650.
- [36] J.P. Hirth, R.C. Pond, Steps, dislocations and disconnections as interface defects relating to structure and phase transformations, Acta Mater. 44 (1996) 4749–4763. https://doi.org/10.1016/S1359-6454(96)00132-2.

- [37] M. Nishida, T. Hara, M. Matsuda, S. Ii, Crystallography and morphology of various interfaces in Ti–Ni, Ti–Pd and Ni–Mn–Ga shape memory alloys, Mater. Sci. Eng. A. 481–482 (2008) 18–27. https://doi.org/10.1016/j.msea.2007.01.179.
- [38] R.C. Pond, J.P. Hirth, Topological model of type II deformation twinning, Acta Mater. 151 (2018) 229–242. https://doi.org/10.1016/j.actamat.2018.03.014.
- [39] R.C. Pond, J.P. Hirth, K.M. Knowles, Topological model of type II deformation twinning in Ni-Ti martensite, Philos. Mag. 99 (2019) 1619–1632. https://doi.org/10.1080/14786435.2019.1587185.
- [40] P.J. Webster, K.R.A. Ziebeck, S.L. Town, M.S. Peak, Magnetic order and phase transformation in Ni ₂ MnGa, Philos. Mag. B. 49 (1984) 295–310. https://doi.org/10.1080/13642817408246515.
- [41] C. Jiang, Y. Muhammad, L. Deng, W. Wu, H. Xu, Composition dependence on the martensitic structures of the Mn-rich NiMnGa alloys, Acta Mater. 52 (2004) 2779–2785. https://doi.org/10.1016/j.actamat.2004.02.024.
- [42] G. Mogylnyy, I. Glavatskyy, N. Glavatska, O. Söderberg, Y. Ge, V.K. Lindroos, Crystal structure and twinning in martensite of Ni1.96Mn1.18Ga0.86 magnetic shape memory alloy, Scr. Mater. 48 (2003) 1427–1432. https://doi.org/10.1016/S1359-6462(03)00108-8.
- [43] L. Righi, F. Albertini, L. Pareti, A. Paoluzi, G. Calestani, Commensurate and incommensurate "5M" modulated crystal structures in Ni–Mn–Ga martensitic phases, Acta Mater. 55 (2007) 5237–5245. https://doi.org/10.1016/j.actamat.2007.05.040.
- [44] J. Pons, R. Santamarta, V.A. Chernenko, E. Cesari, Long-period martensitic structures of Ni-Mn-Ga alloys studied by high-resolution transmission electron microscopy, J. Appl. Phys. 97 (2005) 083516. https://doi.org/10.1063/1.1861137.
- [45] R.C. Pond, J.P. Hirth, Defects at Surfaces and Interfaces, in: Solid State Phys., Elsevier, 1994: pp. 287–365. https://doi.org/10.1016/S0081-1947(08)60641-4.
- [46] R.C. Pond, Line defects in interfaces, in: Dislocations Solids, Elsevier Science Publishers, Amsterdam, 1988: pp. 1–66.
- [47] H. Seiner, R. Chulist, W. Maziarz, A. Sozinov, O. Heczko, L. Straka, Non-conventional twins in five-layer modulated Ni-Mn-Ga martensite, Scr. Mater. 162 (2019) 497–502. https://doi.org/10.1016/j.scriptamat.2018.12.020.
- [48] R.C. Pond, B. Muntifering, P. Müllner, Deformation twinning in Ni2MnGa, Acta Mater. 60 (2012) 3976–3984. https://doi.org/10.1016/j.actamat.2012.03.045.
- [49] T. Braisaz, High-resolution electron microscopy study of the (1012) twin and defects analysis in deformed polycrystalline alpha titanium, Philos. Mag. Lett. 74 (1996) 331–338. https://doi.org/10.1080/095008396180056.
- [50] T. Braisaz, P. Ruterana, G. Nouet, R.C. Pond, Investigation of {1012} twins in Zn using high-resolution electron microscopy: Interfacial defects and interactions, Philos. Mag. A. 75 (1997) 1075–1095. https://doi.org/10.1080/01418619708214012.
- [51] A. Ostapovets, J. Buršík, R. Gröger, Deformation due to migration of faceted {101⁻2} twin boundaries in magnesium and cobalt, Philos. Mag. 95 (2015) 4106–4117. https://doi.org/10.1080/14786435.2015.1115134.
- [52] H.A. Khater, A. Serra, R.C. Pond, Atomic shearing and shuffling accompanying the motion of twinning disconnections in Zirconium, Philos. Mag. 93 (2013) 1279–1298. https://doi.org/10.1080/14786435.2013.769071.

- [53] J. Wang, S.K. Yadav, J.P. Hirth, C.N. Tomé, I.J. Beyerlein, Pure-Shuffle Nucleation of Deformation Twins in Hexagonal-Close-Packed Metals, Mater. Res. Lett. 1 (2013) 126–132. https://doi.org/10.1080/21663831.2013.792019.
- [54] R.C. Pond, J.P. Hirth, A. Serra, D.J. Bacon, Atomic displacements accompanying deformation twinning: shears and shuffles, Mater. Res. Lett. 4 (2016) 185–190. https://doi.org/10.1080/21663831.2016.1165298.
- [55] P. Müllner, C. Solenthaler, The shape of a blocked deformation twin, Philos. Mag. Lett. 69 (1994) 171–175. https://doi.org/10.1080/09500839408241588.
- [56] S.V. Kamat, J.P. Hirth, P. Müllner, The effect of stress on the shape of a blocked deformation twin, Philos. Mag. A. 73 (1996) 669–680. https://doi.org/10.1080/01418619608242989.
- [57] Y. Liu, Z.L. Xie, Twinning and detwinning of <011> type II twin in shape memory alloy, Acta Mater. 51 (2003) 5529–5543. https://doi.org/10.1016/S1359-6454(03)00417-8.
- [58] Y. Liu, Z.L. Xie, The rational nature of type II twin in Ni-Ti shape memory alloy, J. Intell. Mater. Syst. Struct. 17 (2006) 1083–1090. https://doi.org/10.1177/1045389X06064887.
- [59] H. Yan, C. Zhang, Y. Zhang, X. Wang, C. Esling, X. Zhao, L. Zuo, Crystallographic insights into Ni–Co–Mn–In metamagnetic shape memory alloys, J. Appl. Crystallogr. 49 (2016) 1585–1592. https://doi.org/10.1107/S1600576716012140.
- [60] A.S.K. Mohammed, H. Sehitoglu, Modeling the interface structure of type II twin boundary in B19' Ni-Ti from an atomistic and topological standpoint, Acta Mater. 183 (2020) 93–109. https://doi.org/10.1016/j.actamat.2019.10.048.
- [61] L. Straka, A. Soroka, H. Seiner, H. Hänninen, A. Sozinov, Temperature dependence of twinning stress of type I and type II twins in 10M modulated Ni–Mn–Ga martensite, Scr. Mater. 67 (2012) 25–28. https://doi.org/10.1016/j.scriptamat.2012.03.012.
- [62] O. Heczko, L. Straka, H. Seiner, Different microstructures of mobile twin boundaries in 10M modulated Ni–Mn–Ga martensite, Acta Mater. 61 (2013) 622–631. https://doi.org/10.1016/j.actamat.2012.10.007.
- [63] L. Straka, N. Lanska, K. Ullakko, A. Sozinov, Twin microstructure dependent mechanical response in Ni–Mn–Ga single crystals, Appl. Phys. Lett. 96 (2010) 131903. https://doi.org/10.1063/1.3373608.
- [64] Y. Ge, O. Söderberg, N. Lanska, A. Sozinov, K. Ullakko, V.K. Lindroos, Crystal structure of three Ni-Mn-Ga alloys in powder and bulk materials, J. Phys. IV Proc. 112 (2003) 921–924. https://doi.org/10.1051/jp4:20031031.
- [65] O. Heczko, Magnetic shape memory effect and highly mobile twin boundaries, Mater. Sci. Technol. 30 (2014) 1559–1578. https://doi.org/10.1179/1743284714Y.0000000599.
- [66] M. Matsuda, Y. Yasumoto, K. Hashimoto, T. Hara, M. Nishida, Transmission electron microscopy of twins in 10M martensite in Ni-Mn-Ga ferromagnetic shape memory alloy, Mater. Trans. 53 (2012) 902–906. https://doi.org/10.2320/matertrans.M2012002.
- [67] T. Onda, Y. Bando, T. Ohba, K. Otsuka, Electron Microscopy Study of Twins in Martensite in a Ti-50.0 at%Ni Alloy, Mater. Trans. JIM. 33 (1992) 354–359. https://doi.org/10.2320/matertrans1989.33.354.
- [68] P. Müllner, Twinning stress of type I and type II deformation twins, Acta Mater. 176 (2019) 211–219. https://doi.org/10.1016/j.actamat.2019.07.004.

- [69] K.M. Knowles, D.A. Smith, The crystallography of the martensitic transformation in equiatomic nickel-titanium, Acta Metall. 29 (1981) 101–110. https://doi.org/10.1016/0001-6160(81)90091-2.
- [70] J.P. Hirth, R.C. Pond, J. Lothe, Disconnections in tilt walls, Acta Mater. 54 (2006) 4237–4245. https://doi.org/10.1016/j.actamat.2006.05.017.
- [71] J.P. Hirth, R.C. Pond, J. Lothe, Spacing defects and disconnections in grain boundaries, Acta Mater. 55 (2007) 5428–5437. https://doi.org/10.1016/j.actamat.2007.06.004.
- [72] E. Faran, D. Shilo, Dynamics of twin boundaries in ferromagnetic shape memory alloys, Mater. Sci. Technol. 30 (2014) 1545–1558. https://doi.org/10.1179/1743284714Y.0000000570.
- [73] E. Faran, D. Shilo, Ferromagnetic shape memory alloys—challenges, applications, and experimental characterization, Exp. Tech. 40 (2016) 1005–1031. https://doi.org/10.1007/s40799-016-0098-5.
- [74] A. Saren, T. Nicholls, J. Tellinen, K. Ullakko, Direct observation of fast-moving twin boundaries in magnetic shape memory alloy Ni–Mn–Ga 5M martensite, Scr. Mater. 123 (2016) 9–12. https://doi.org/10.1016/j.scriptamat.2016.04.004.
- [75] A. Saren, K. Ullakko, Dynamic twinning stress and viscous-like damping of twin boundary motion in magnetic shape memory alloy Ni-Mn-Ga, Scr. Mater. 139 (2017) 126–129. https://doi.org/10.1016/j.scriptamat.2017.06.010.
- [76] A.A. Likhachev, K. Ullakko, Magnetic-field-controlled twin boundaries motion and giant magneto-mechanical effects in Ni–Mn–Ga shape memory alloy, Phys. Lett. A. 275 (2000) 142–151. https://doi.org/10.1016/s0375-9601(00)00561-2.
- [77] M. Veligatla, C.J. Garcia-Cervera, P. Müllner, Magnetic domain-twin boundary interactions in Ni–Mn–Ga, Acta Mater. 193 (2020) 221–228. https://doi.org/10.1016/j.actamat.2020.03.045.
- [78] A. Saren, A. Sozinov, S. Kustov, K. Ullakko, Stress-induced a/b compound twins redistribution in 10M Ni-Mn-Ga martensite, Scr. Mater. 175 (2020) 11–15. https://doi.org/10.1016/j.scriptamat.2019.09.001.
- [79] P.M. Anderson, J.P. Hirth, J. Lothe, Theory of dislocations, Cambridge University Press, 2017.
- [80] R.C. Pond, A. Serra, D.J. Bacon, Dislocations in interfaces in the h.c.p. metals—II. Mechanisms of defect mobility under stress, Acta Mater. 47 (1999) 1441–1453. https://doi.org/10.1016/s1359-6454(99)00017-8.
- [81] A. Serra, D.J. Bacon, A new model for 1012 twin growth in hcp metals, Philos. Mag. A. 73 (1996) 333–343. https://doi.org/10.1080/01418619608244386.
- [82] A. Serra, D.J. Bacon, A model for simulating the motion of line defects in twin boundaries in HCP metals, Z. Für Met. 95 (2004) 242–243. https://doi.org/10.3139/146.017942.
- [83] H.A. Khater, A. Serra, R.C. Pond, Atomic shearing and shuffling accompanying the motion of twinning disconnections in Zirconium, Philos. Mag. 93 (2013) 1279–1298. https://doi.org/10.1080/14786435.2013.769071.
- [84] N. Zreihan, E. Faran, D. Shilo, The effect of loading rate on characteristics of type II twin boundary motion in Ni-Mn-Ga, Scr. Mater. 144 (2018) 44–47. https://doi.org/10.1016/j.scriptamat.2017.09.045.

- [85] B.J. Karki, Y. Behar, I. Harel, E. Caplan, A. Sabbag, D. Shilo, P. Mullner, E. Faran, A simple method to characterize high rate twin boundary kinetics in Ni-Mn-Ga, Rev. Sci. Instrum. 90 (2019) 105107. https://doi.org/10.1063/1.5109934.
- [86] W.T. Read, W. Shockley, Dislocation Models of Crystal Grain Boundaries, Phys. Rev. 78 (1950) 275–289. https://doi.org/10.1103/PhysRev.78.275.
- [87] L. Straka, A. Sozinov, J. Drahokoupil, V. Kopecký, H. Hänninen, O. Heczko, Effect of intermartensite transformation on twinning stress in Ni-Mn-Ga 10M martensite, J. Appl. Phys. 114 (2013) 063504. https://doi.org/10.1063/1.4817717.
- [88] T. Hahn, International Tables of Crystallography, A, 854 p. D, Reidel Publishing Company, Dordrecht, 1983.
- [89] J.P. Hirth, R.C. Pond, R.G. Hoagland, X.-Y. Liu, J. Wang, Interface defects, reference spaces and the Frank–Bilby equation, Prog. Mater. Sci. 58 (2013) 749–823. https://doi.org/10.1016/j.pmatsci.2012.10.002.
- [90] A. Armstrong, A. Saren, Private communication.